

Merger of binary neutron stars to a black hole: Disk mass, short gamma-ray bursts, and quasinormal mode ringing

Masaru Shibata¹ and Keisuke Taniguchi²

¹*Graduate School of Arts and Sciences, University of Tokyo, Komaba, Meguro, Tokyo 153-8902, Japan*

²*Department of Physics, University of Illinois at Urbana-Champaign, Urbana, IL 61801-3080, USA*

Three-dimensional simulations for the merger of binary neutron stars are performed in the framework of full general relativity. We pay particular attention to the black hole formation case and to the resulting mass of the surrounding disk for exploring possibility for formation of the central engine of short-duration gamma-ray bursts (SGRBs). Hybrid equations of state are adopted mimicking realistic, stiff nuclear equations of state (EOSs), for which the maximum allowed gravitational mass of cold and spherical neutron stars, M_{sph} , is larger than $2M_{\odot}$. Such stiff EOSs are adopted motivated by the recent possible discovery of a heavy neutron star of mass $\sim 2.1 \pm 0.2M_{\odot}$. For the simulations, we focus on binary neutron stars of the ADM mass $M \gtrsim 2.6M_{\odot}$. For an ADM mass larger than the threshold mass M_{thr} , the merger results in prompt formation of a black hole irrespective of the mass ratio Q_M with $0.65 \lesssim Q_M \leq 1$. The value of M_{thr} depends on the EOSs and is approximately written as $1.3\text{--}1.35M_{\text{sph}}$ for the chosen EOSs. For the black hole formation case, we evolve the spacetime using a black hole excision technique and determine the mass of a quasistationary disk surrounding the black hole. The disk mass steeply increases with decreasing the value of Q_M for given ADM mass and EOS. This suggests that a merger with small value of Q_M is a candidate for producing central engine of SGRBs. For $M < M_{\text{thr}}$, the outcome is a hypermassive neutron star of a large ellipticity. Because of the nonaxisymmetry, angular momentum is transported outward. If the hypermassive neutron star collapses to a black hole after the longterm angular momentum transport, the disk mass may be $\gtrsim 0.01M_{\odot}$ irrespective of Q_M . Gravitational waves are computed in terms of a gauge-invariant wave extraction technique. In the formation of the hypermassive neutron star, quasiperiodic gravitational waves of frequency between 3 and 3.5 kHz are emitted irrespective of EOSs. The effective amplitude of gravitational waves can be $\gtrsim 5 \times 10^{-21}$ at a distance of 50 Mpc, and hence, it may be detected by advanced laser-interferometers. For the black hole formation case, the black hole excision technique enables a longterm computation and extraction of ring-down gravitational waves associated with a black hole quasinormal mode. It is found that the frequency and amplitude are $\approx 6.5\text{--}7$ kHz and $\sim 10^{-22}$ at a distance of 50 Mpc for the binary of mass $M \approx 2.7\text{--}2.9M_{\odot}$.

PACS numbers: 04.25.Dm, 04.30.-w, 04.40.Dg

I. INTRODUCTION

Binary neutron stars in close orbits are strong emitters of gravitational waves. A scenario based mainly on a recent discovery of the binary system PSR J0737-3039 [1] suggests that the detection rate of gravitational waves by the advanced laser-interferometric gravitational wave observatory (LIGO) will be $\sim 40\text{--}600 \text{ yr}^{-1}$ [2]; i.e., one event per year is expected within the distance of $\approx 35\text{--}90$ Mpc since the advanced LIGO is able to detect gravitational waves from coalescing binary neutron stars within the distance of about 300 Mpc. This indicates that a coalescing and merging binary neutron star is one of the most promising sources for kilometer-size laser-interferometric detectors [3, 4].

Merger of binary neutron stars has been also proposed for many years [5, 6] as a possible formation scenario for a central engine of short-hard gamma-ray bursts (SGRBs). Associations between SGRBs and elliptical galaxies reported recently [7] make it unlikely that SGRBs are related to supernova stellar core collapse since elliptical galaxies have not produced massive stars in the past $\sim 10^{10}$ yrs. In addition, recent observations of the afterglow of the SGRB 050709 rule out the presence of a

supernova light curve and point to a binary compact object merger as the most likely central engine [8, 9]. The merger of compact-object binaries (binary neutron stars or black hole-neutron star binaries) is thus the most favored hypothesis for explaining SGRBs. According to a standard scenario based on the merger hypothesis, after the merger, a stellar-mass black hole is formed with a surrounding accretion torus of mass $\gtrsim 0.01M_{\odot}$ [10]. Energy extracted from this system by either magnetohydrodynamic processes or neutrino radiation powers the fireball and high-Lorentz factor jets for SGRBs, for which the typical burst energy is between 10^{48} and 10^{49} ergs (after a correction of a beaming factor) [8].

Hydrodynamic simulations in the framework of full general relativity provide the best approach for studying the merger of binary neutron stars. Over the last several years, numerical methods for solving coupled equations of the Einstein and hydrodynamic equations have been developed (e.g., [11, 12, 13, 14, 15, 16, 17, 18, 19, 20, 21]) and now such simulations are feasible with an accuracy high enough for yielding scientific results (e.g., [17, 21]).

For many years, the fully general relativistic (GR) simulations for the merger of binary neutron stars had been performed adopting an ideal equation of state (EOS)

$P = (\Gamma - 1)\rho\epsilon$ where P , ρ , ϵ , and Γ are pressure, rest-mass density, specific internal energy, and adiabatic constant [12, 13, 17, 18, 19]. However, simulations with realistic EOSs are necessary for quantitative understanding for the merger. From this motivation, in a previous paper, we performed simulations taking into account realistic nuclear EOSs [21] and clarified that properties of the outcomes and gravitational waveforms are significantly different from those obtained in the ideal EOS with $\Gamma = 2$. In particular, we found that a hypermassive neutron star [22, 23] of *elliptical shape* is formed for a reasonable mass range of the merger progenitor because of the stiffness of the realistic EOSs. As a consequence, hypermassive neutron stars can be strong emitters of high-frequency, quasiperiodic gravitational waves, which may be detected by the advanced laser-interferometric gravitational wave detectors [24].

In this paper, we extend the previous work from the following motivation. One is based on the recent possible discovery of a high-mass neutron star with mass $2.1 \pm 0.2M_\odot$ (one σ error) [25]. This measurement indicates that the maximum mass of spherical neutron stars, M_{sph} , may be larger than $\sim 2M_\odot$, and hence, very stiff EOSs such as those proposed in [26, 27] are favored. In particular, if M_{sph} is larger than $\sim 2.1M_\odot$, the nuclear EOS is so stiff that most of the EOSs proposed so far will be rejected, resulting in that restricted EOSs such as those derived by Akmal, Pandharipande, and Ravenhall (hereafter APR) [26] survive. However, fully GR simulations for the merger with such stiff EOSs have not been performed to this time. This paper is mainly devoted to presenting new numerical results obtained with the APR EOS.

The other motivation is to determine the final outcome for the case that a black hole is formed promptly after the merger. Clarifying the final state of the black hole system, in particular the surrounding disk mass, is an important subject in exploring whether a remnant of the merger can be a central engine of SGRBs. The previous simulations [17, 21] were performed only for a short time after the formation of black hole because of the so-called grid stretching around the black hole horizon. Under this situation, the geometry is so steep near the horizon that the accuracy in the numerical computation is lost. The popular approach for overcoming this difficulty is to adopt excision techniques [28, 29, 30]. In the present simulation, the growth of the black hole is followed until the system approximately reaches a relaxed state by employing a simple excision technique [29, 30]. With this technique, the disk mass surrounding a black hole can be determined. Simulations are performed for a wide variety of mass ratio for the black hole formation case as well as in two EOSs. We show that the disk mass surrounding a black hole depends strongly on the mass ratio of the binary. In addition, the excision technique enables a simulation long enough to extract gravitational waves emitted after the formation of black holes. We show for the first time that gravitational waves are determined by

a quasinormal mode of the formed black hole.

To determine the disk mass around a formed black hole, Oechslin and Janka recently performed a series of interesting simulations for merger of binary neutron stars [31] using a realistic EOS (the so-called Shen's EOS) [32], which is also so stiff that the maximum mass of spherical neutron stars is $\approx 2.2M_\odot$. They employ an approximate formulation of general relativity (the conformal flatness approximation for the spatial three-geometry). In this approximation, gravitational radiation is neglected. They follow the merger process only in the formation of hypermassive neutron stars. Assuming that the hypermassive neutron stars eventually collapse to a black hole by a dissipation mechanism, they estimate the disk mass (i.e., they compute the rest-mass of fluid elements with the sufficiently large specific angular momentum which are expected to escape falling into the black hole). They conclude that the disk mass around the formed black hole will be always larger than $0.02M_\odot$ because the angular momentum transport during the merger process efficiently works. As shown in Sec. IV, the angular momentum transport indeed plays an important role in the formation of disks around the hypermassive neutron stars, and hence, our numerical results agree partly with theirs. However, for the merger of high-mass binaries, our results do not agree with theirs.

In their case, the merger results in a hypermassive neutron star even for the total gravitational mass $\approx 3M_\odot$. This result disagrees with ours. The reason may be partly due to different choice of the EOS from ours, but is also likely due to the fact that they do not take into account radiation reaction of gravitational waves. As shown in Sec. V as well as in [21], angular momentum is dissipated by a factor of $\sim 15\%$ in the first 3 ms from the last one orbit. This significant dissipation induces prompt collapse to a black hole for the high-mass case in our results. In this case, a black hole is formed in much shorter than 1 ms after the onset of the merger, and hence, the angular momentum transport does not work efficiently before the black hole formation, unless the mass difference of two stars is significant. We find that the disk mass is much smaller than $0.01M_\odot$ in the prompt formation of a black hole for the nearly equal-mass case, as shown in Sec. IV.

The paper is organized as follows. In Sec. II A–D, basic equations, gauge conditions, excision scheme, methods for extracting gravitational waves, and quantities used in the analysis for numerical results are reviewed. Then, the hybrid EOSs adopted in this paper are described in Sec. II E. In Sec. III, initial conditions and setting for simulations are described. In Sec. IV, numerical results are shown, paying attention to the merger process, the formed outcome, and the disk mass surrounding a black hole. Implication of our results to formation of a central engine of SGRBs is also discussed in IV D. In Sec. V, gravitational waveforms are presented. Section VI is devoted to a summary. Throughout this paper, we adopt the geometrical units in which

$G = c = 1$ where G and c are the gravitational constant and the speed of light. Latin and Greek indices denote spatial components (x, y, z) and space-time components (t, x, y, z) , respectively: $r \equiv \sqrt{x^2 + y^2 + z^2}$. $\delta_{ij} (= \delta^{ij})$ denotes the Kronecker delta.

II. FORMULATION

A. Summary of formulation

Our formulation and numerical scheme for fully GR simulations in three spatial dimensions are the same as in [17, 21], to which the reader may refer for details of basic equations.

The fundamental variables for geometry are α : lapse function, β^k : shift vector, γ_{ij} : metric in three-dimensional spatial hypersurface, and K_{ij} : extrinsic curvature. In addition, we define the conformal factor $\psi \equiv e^\phi \equiv \gamma^{1/12}$, conformal three-metric $\tilde{\gamma}_{ij} = e^{-4\phi}\gamma_{ij}$, three auxiliary functions $F_i \equiv \delta^{jk}\partial_j\tilde{\gamma}_{ik}$, the trace of the extrinsic curvature K , and a tracefree part of the extrinsic curvature $\hat{A}_{ij} \equiv e^{-4\phi}(K_{ij} - \gamma_{ij}K/3)$. Here, $\gamma = \det(\gamma_{ij})$.

The Einstein evolution equations are solved using a version of the BSSN formalism following previous papers [11, 13, 17, 33]: We evolve $\tilde{\gamma}_{ij}$, ϕ , F_i , \hat{A}_{ij} , and K using an unconstrained free evolution code. The latest version of our formulation and numerical method is described in [17]. The point worthy to note is that the equation for ϕ is written to a conservative form similar to the continuity equation, and solving this improves the accuracy of the conservation of the ADM (Arnowitt-Deser-Misner) mass and the total angular momentum significantly.

The fundamental variables for the hydrodynamics are ρ : rest-mass density, ε : specific internal energy, P : pressure, u^μ : four velocity, and

$$v^i = \frac{dx^i}{dt} = \frac{u^i}{u^t}. \quad (1)$$

For our numerical implementation of the hydrodynamic equations, we define a weighted density, a weighted four-velocity, and a specific energy defined, respectively, by

$$\rho_* \equiv \rho \alpha u^t e^{6\phi}, \quad (2)$$

$$\hat{u}_i \equiv h u_i, \quad (3)$$

$$\hat{e} \equiv h \alpha u^t - \frac{P}{\rho \alpha u^t}, \quad (4)$$

where $h = 1 + \varepsilon + P/\rho$ denotes the specific enthalpy. GR hydrodynamic equations are written into the conservative form for variables ρ_* , $\rho_* \hat{u}_i$, and $\rho_* \hat{e}$, and solved using a high-resolution central (HRC) scheme [34, 35]. In this approach, the transport terms such as $\partial_i(\dots)$ are computed by Kurganov-Tadmor scheme with a third-order (piecewise parabolic) spatial interpolation. In [35], we

illustrate that the results obtained in this scheme approximately agree with those in a high-resolution shock-capturing scheme based on the Roe-type reconstruction for the fluxes [15, 16]. At each time step, αu^t is determined by solving an algebraic equation derived from the normalization $u^\mu u_\mu = -1$, and then, the primitive variables such as ρ , ε , and v^i are updated.

A uniform atmosphere of small density $\rho \approx 10^7 \text{ g/cm}^3$ is added outside neutron stars at $t = 0$, since the vacuum is not allowed in any shock-capturing scheme. However, in the HRC scheme, the density can be chosen to be much smaller than the previous values [17, 21]. This is a benefit in this scheme. The integrated baryon rest-mass of the atmosphere is $\sim 10^{-4} M_\odot$ in the present simulation with the largest grid size (see Sec. III). Hence, the effect of the atmosphere for the evolution of binary neutron stars and its contribution to the disk mass around a black hole eventually formed is negligible. (However, for the nearly equal-mass merger, the disk mass surrounding a black hole is small as several $\times 10^{-4} M_\odot$; see Sec. IV B 3. In such case, we subtract the contribution of the atmosphere.)

As the time slicing condition, an approximate maximal slice (AMS) condition $K \approx 0$ has been adopted following previous papers [11, 13, 36] to this time. In this condition, α is determined by approximately solving an elliptic-type equation. This condition is also adopted in the case of hypermassive neutron star formation in this paper. On the other hand, for the formation of a black hole in which an excision evolution is necessary to follow its growth, the AMS condition is not advantageous since it is not easy to find an appropriate boundary condition for α at the excision surface. Thus, for the black hole formation, we adopt a dynamical time slicing in which the lapse function is determined from

$$\partial_t \alpha = -\alpha K. \quad (5)$$

In this condition, we need to determine the initial value of α . Here, we initially impose the maximal slicing condition for α . A few simulations were performed in both slicing conditions until formation of a black hole, and we confirmed that the results depend weakly on the slicing conditions, indicating that Eq. (5) gives a similar slicing to the maximal slicing.

As the spatial gauge condition, we adopt the following hyperbolic gauge condition as in [17, 37];

$$\partial_t \beta^k = \tilde{\gamma}^{kl}(F_l + \Delta t \partial_t F_l). \quad (6)$$

Here, Δt denotes a time step of the simulation. Successful numerical results for the merger of binary neutron stars in this gauge condition are presented in [17, 21].

In the presence of a black hole, the location is determined using an apparent horizon finder for which our method is described in [38]. The location of the apparent horizons is used for determining an excision surface (see the next subsection).

Following previous works, we adopt binary neutron stars in close quasiequilibrium circular orbits as the initial condition. In computing the quasiequilibrium state, we use the so-called conformally flat formalism for the Einstein equation [39]. Solutions in this formalism satisfy the constraint equations in general relativity, and hence, it can be used for the initial condition. The irrotational velocity field is assumed since it is considered to be a good approximation for coalescing binary neutron stars in nature [40]. The coupled equations of the field and hydrostatic equations [41] are solved by a spectral method developed by Bonazzola, Gourgoulhon, and Marck [42]. Detailed numerical calculations have been done by Taniguchi and part of the numerical results are presented in [43].

B. Black hole excision

Whenever an apparent horizon is found during the simulation, subsequent evolution is followed using an excision technique [28]. We adopt the so-called simple excision method originally proposed by Alcubierre and Brügmann [29]. In this method, one first determines a two-surface inside an apparent horizon which is used for the inner boundary in the numerical simulation. And then, at the boundary, we impose the so-called copying boundary condition in which the time derivative of geometric variables $\tilde{\gamma}_{ij}$, ϕ , \tilde{A}_{ij} , K , and F_i is assumed to be spatially constant at the boundary.

In our method, we choose a cube as the excision boundary of which the length of each edge is $2\ell = 2n\Delta x$ where Δx denotes the grid spacing. n is a positive integer determined from the equation

$$n = \text{integer}[\min[r_{\text{AH}}(\theta, \varphi)]/(\sqrt{2}\Delta x)] - 1 \quad (7)$$

where $r_{\text{AH}}(\theta, \varphi)$ denotes the coordinate radii of the apparent horizon. At the surface of the cube, we simply copy the time derivative of each variable at the next cell along the normal line of each surface. At the corners, we copy the time derivative at the next cell along the line connecting the corner and origin, and at the edges, at the next cell along a perpendicular line connecting the edge and another edge in the diagonal direction.

Since the computational resource is restricted, the radii of the apparent horizon are covered only by 6–8 grid zones. As a result, the value of n is small; typically $n = 2$. With such a small value, it is difficult to maintain the accuracy for a long time. However, it is still possible to continue the simulation for ~ 0.5 – 0.7 ms after formation of a black hole, which is sufficiently long for approximately determining the disk mass around the black hole, and for computing ring-down gravitational waveforms associated with a black hole quasinormal mode.

C. Extracting gravitational waves

Gravitational waves are computed in terms of the gauge-invariant Moncrief variables in a flat spacetime [44] as in our series of papers (e.g., [17, 21, 36, 45]). The detailed equations are describe in [17, 45] to which the reader may refer. In this method, we split the metric in the wave zone into the flat background and linear perturbation. Then, the linear part is decomposed using the tensor spherical harmonics and gauge-invariant variables are constructed for each mode of eigen values (l, m) . The gauge-invariant variables of $l \geq 2$ can be regarded as gravitational waves in the wave zone, and hence, we focus on such modes. In the merger of binary neutron stars of mass ratio larger than ~ 0.7 , we have found that the even-parity mode of $(l, |m|) = (2, 2)$ is much larger than other modes. Thus, in the following, we pay attention only to this mode.

Using the gauge-invariant variables, the luminosity and the angular momentum flux of gravitational waves can be defined by

$$\frac{dE}{dt} = \frac{r^2}{32\pi} \sum_{l,m} |\partial_t R_{lm}|^2 \quad (8)$$

$$\frac{dJ}{dt} = \frac{r^2}{32\pi} \sum_{l,m} |m(\partial_t R_{lm})R_{lm}|, \quad (9)$$

where R_{lm} is the gauge-invariant variable. In this paper, we focus only on the even-parity mode with $l = 2$ for R_{lm} . The total radiated energy and angular momentum are obtained by the time integration of dE/dt and dJ/dt .

To search for the characteristic frequencies of gravitational waves, the Fourier spectra are computed by

$$\bar{R}_{lm}(f) = \int e^{2\pi i f t} R_{lm}(t) dt, \quad (10)$$

where f denotes a frequency of gravitational waves. Using the Fourier spectrum, the energy power spectrum is defined by

$$\frac{dE}{df} = \frac{\pi}{4} r^2 \sum_{l \geq 2, m \geq 0} |\bar{R}_{lm}(f)f|^2 \quad (f > 0), \quad (11)$$

where for $m \neq 0$, we define

$$\bar{R}_{lm}(f) \equiv \sqrt{|\bar{R}_{lm}(f)|^2 + |\bar{R}_{l-m}(f)|^2} \quad (m > 0), \quad (12)$$

and use $|\bar{R}_{lm}(-f)| = |\bar{R}_{lm}(f)|$ for deriving Eq. (11).

Since we focus only on the $l = 2$ even-parity mode, the gravitational waveforms are written as

$$h_+ = \frac{1}{r} \left[\sqrt{\frac{5}{64\pi}} \{ R_{22+}(1 + \cos^2 \theta) \cos(2\varphi) + R_{22-}(1 + \cos^2 \theta) \sin(2\varphi) \} + \sqrt{\frac{15}{64\pi}} R_{20} r \sin^2 \theta \right], \quad (13)$$

$$h_{\times} = \frac{2}{r} \sqrt{\frac{5}{64\pi}} \left[-R_{22+} \cos \theta \sin(2\varphi) + R_{22-} \cos \theta \cos(2\varphi) \right]. \quad (14)$$

In Eqs. (13) and (14), the variables are defined by

$$R_{22\pm} \equiv \frac{R_{22} \pm R_2}{\sqrt{2}} r. \quad (15)$$

In the following, we present

$$R_+ = \sqrt{\frac{5}{16\pi}} R_{22+}, \quad R_{\times} = \sqrt{\frac{5}{16\pi}} R_{22-}. \quad (16)$$

These have the unit of length and provide the amplitude of a given mode measured by an observer located in the most optimistic direction. The amplitude of gravitational waves, h_{gw} , observed at a distance of r along the optimistic direction ($\theta = 0$) is written as

$$h_{\text{gw}} \approx 10^{-22} \left(\frac{\sqrt{R_+^2 + R_{\times}^2}}{0.31 \text{ km}} \right) \left(\frac{100 \text{ Mpc}}{r} \right). \quad (17)$$

D. Definitions of quantities and methods for calibration

In numerical simulations, we refer to the total baryon rest-mass, the ADM mass, and the angular momentum of the system, which are given by

$$M_* \equiv \int \rho_* d^3x = \text{const}, \quad (18)$$

$$\begin{aligned} M &\equiv -\frac{1}{2\pi} \oint_{r \rightarrow \infty} \partial_i \psi dS_i \\ &= \int \left[\rho_{\text{H}} e^{5\phi} + \frac{e^{5\phi}}{16\pi} \left(\tilde{A}_{ij} \tilde{A}^{ij} - \frac{2}{3} K^2 \right. \right. \\ &\quad \left. \left. - \tilde{R}_k^k e^{-4\phi} \right) \right] d^3x, \end{aligned} \quad (19)$$

$$\begin{aligned} J &\equiv \frac{1}{8\pi} \oint_{r \rightarrow \infty} \varphi^i \tilde{A}_i^j e^{6\phi} dS_j \\ &= \int e^{6\phi} \left[J_i \varphi^i + \frac{1}{8\pi} \left(\tilde{A}_i^j \partial_j \varphi^i - \frac{1}{2} \tilde{A}_{ij} \varphi^k \partial_k \tilde{\gamma}^{ij} \right. \right. \\ &\quad \left. \left. + \frac{2}{3} \varphi^j \partial_j K \right) \right] d^3x, \end{aligned} \quad (20)$$

where $dS_j = r^2 \partial_j r d(\cos \theta) d\varphi$, $\varphi^j = -y(\partial_x)^j + x(\partial_y)^j$, $\rho_{\text{H}} = \rho \alpha u^t \hat{e}$, $J_i = \rho \hat{u}_i$, and \tilde{R}_k^k denotes the Ricci scalar with respect to $\tilde{\gamma}_{ij}$. To derive the expressions for M and J in the form of volume integral, the Gauss law is used.

The notations M_{*1} and M_{*2} are used to denote the baryon rest-mass of the primary and secondary neutron stars, respectively. In terms of them, the baryon rest-mass ratio is defined by $Q_M \equiv M_{*2}/M_{*1} (\leq 1)$.

In numerical simulation, M and J are computed using the volume integral shown in Eqs. (19) and (20).

Since the computational domain is finite, they are not constant and decrease after gravitational waves propagate away from the computational domain. Therefore, for $t > 0$, M and J are not equal to the ADM mass and the total angular momentum defined at spatial infinity, but quasilocal quantities. However, in this paper, we refer to them simply as the ADM mass and the total angular momentum.

The decrease rates of M and J should be equal to the emission rates of the energy and the angular momentum by gravitational radiation according to the conservation law. Denoting the radiated energy and angular momentum from the beginning of the simulation to the time t as $\Delta E(t)$ and $\Delta J(t)$, the conservation relations are

$$M(t) + \Delta E(t) = M_0, \quad (21)$$

$$J(t) + \Delta J(t) = J_0, \quad (22)$$

where M_0 and J_0 are the initial values of M and J . We check that these conservation laws approximately hold during the simulation.

During merger of binary neutron stars (from the last one orbit to a relaxed state formed after the merger), the angular momentum is dissipated by 15–30% (cf. Sec. V). Obviously, the dissipation effect plays a crucial role in determining the final outcome. Therefore, checking that Eq. (22) holds in a simulation is one of the most important procedures to confirm that the numerical results are reliable.

In addition to checking the conservation of the mass and the angular momentum, we monitor the violation of the Hamiltonian constraint in the same manner as in [16, 17, 21] in the absence of black hole. In its presence, the violation is defined for a region outside the excision surface. As demonstrated in [17, 21], the typical magnitude of the violation is of order 1% throughout the simulation in the absence of black hole. In its presence, the violation is amplified. However, the typical magnitude is still $\sim 10\%$ in the early phase of the excision run. The magnitude gradually increases until the crash of computation.

E. Equations of state

Following [21], we adopt a hybrid EOS for modeling neutron stars' EOS; namely, we write the pressure and the specific internal energy in the form

$$P = P_{\text{cold}} + P_{\text{th}}, \quad (23)$$

$$\varepsilon = \varepsilon_{\text{cold}} + \varepsilon_{\text{th}}. \quad (24)$$

Here P_{cold} and $\varepsilon_{\text{cold}}$ are the cold (zero-temperature) parts, and are written as a function of ρ . For them, we assign realistic EOSs for zero-temperature nuclear matter. In this paper, we adopt the APR [26] and SLy (Skyrme-Lyon) EOSs [27]. These are tabulated as a function of the baryon rest-mass density for a wide density range

i	p_i (SLy)	p_i (APR)	i	p_i (SLy)	p_i (APR)
1	0.1037	0.0889	9	9×10^5	9×10^5
2	0.1956	0.1821	10	4	4
3	39264	5.945×10^5	11	0.75	0.75
4	1.9503	2.4265	12	0.057	0.057
5	254.83	1600.0	13	0.138	0.138
6	1.3823	2.165	14	0.84	0.84
7	-1.234	-6.96	15	0.338	0.338
8	1.2×10^5	1.2×10^5			

TABLE I: The values of p_i in units of $c = G = M_\odot = 1$.

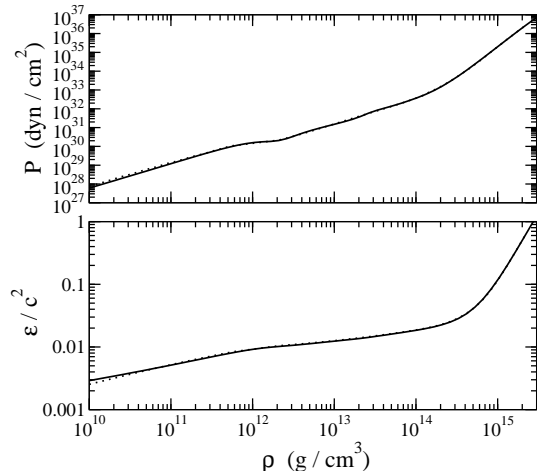


FIG. 1: Pressure and specific internal energy as a function of baryon rest-mass density ρ for the APR EOS. The solid and dotted curves denote the results by fitting formulae and numerical data tabulated, respectively.

from $\sim 10 \text{ g/cm}^3$ to $\sim 10^{16} \text{ g/cm}^3$. To simplify numerical implementation for the simulation, we make fitting formulae from the EOS tables as in [46].

In our approach, we first make a fitting formula for $\varepsilon_{\text{cold}}$ in the form

$$\begin{aligned} \varepsilon_{\text{cold}}(\rho) = & [(1 + p_1\rho^{p_2} + p_3\rho^{p_4})(1 + p_5\rho^{p_6})^{p_7} - 1] \\ & \times f(-p_8\rho + p_{10}) \\ & + p_{12}\rho^{p_{13}}f(p_8\rho - p_{10})f(-p_9\rho + p_{11}) \\ & + p_{14}\rho^{p_{15}}f(p_9\rho - p_{11}), \end{aligned} \quad (25)$$

where $f(x) = 1/(e^x + 1)$, and the constant coefficients p_i ($i=1-15$) are listed in Table I. In making the formulae, we focus only on the density for $\rho \geq 10^{10} \text{ g/cm}^3$, since the matter of lower density does not play an important role in the merger. Then, the pressure is computed from the thermodynamic relation in the zero-temperature limit

$$P_{\text{cold}} = \rho^2 \frac{d\varepsilon_{\text{cold}}}{d\rho}. \quad (26)$$

With this approach, the accuracy of the fitting for the pressure is not as good as that in [46], but the first law

of the thermodynamics is completely satisfied in contrast to the work of [46].

In Fig. 1, we compare P_{cold} and $\varepsilon_{\text{cold}}$ calculated by the fitting formulae (solid curves) with the numerical data tabulated (dotted curves) for the APR EOS [47]. The same figures for the SLy EOS are shown in [21]. It is found that the fitting formulae agree approximately with the tabulated data sets. The relative error between two results is within $\sim 10\%$ for $\rho > 10^{10} \text{ g/cm}^3$ and less than 2% for supranuclear density with $\rho \gtrsim 2 \times 10^{14} \text{ g/cm}^3$.

In Fig. 2, we show the relations among the ADM mass M , the total baryon rest-mass M_* , the central density ρ_c , and the circumferential radius R for cold and spherical neutron stars in the APR and SLy EOSs. The maximum ADM mass (baryon rest-mass) for the APR and SLy EOSs is about 2.18 and $2.04M_\odot$, respectively. It is worthy to note that for the APR EOS, the radius is in a narrow range ($11.2-11.4 \text{ km}$) for the ADM mass from $\sim 0.5M_\odot$ to $\sim 1.7M_\odot$, while for the SLy EOS, it decreases with increasing the ADM mass. This results in the difference on disk formation in the merger of unequal-mass neutron stars.

P_{th} and ε_{th} in Eqs. (23) and (24) are the thermal (finite-temperature) parts. During the simulation, ρ and ε are computed from hydrodynamic variables ρ_* and \hat{e} . Thus, ε_{th} is determined by $\varepsilon - \varepsilon_{\text{cold}}$. The thermal part of the pressure P_{th} is related to the specific thermal energy $\varepsilon_{\text{th}} \equiv \varepsilon - \varepsilon_{\text{cold}}$ as

$$P_{\text{th}} = (\Gamma_{\text{th}} - 1)\rho\varepsilon_{\text{th}}, \quad (27)$$

where Γ_{th} is an adiabatic constant for which we set $\Gamma_{\text{th}} = 2$ taking into account the fact that the EOSs for high-density nuclear matter are stiff. Since $\Gamma_{\text{th}} \approx 5/3$ for the ideal non-relativistic Fermi gas [48], it is reasonable to consider that it is much larger than $5/3$ for the nuclear matter. We note that in [21], we also chose $\Gamma_{\text{th}} = 1.3$ and 1.65 and found that the numerical results depend only weakly on its value.

III. INITIAL CONDITION AND SETTING FOR SIMULATION

In Table II, we summarize several quantities that characterize irrotational binary neutron stars in quasiequilibrium circular orbits used as initial conditions for the present simulations. Since the lifetime of binary neutron stars from the birth to the merger is longer than $\sim 10^8$ yrs for the observed systems [49], the temperature of each neutron star will be very low ($\lesssim 10^5 \text{ K}$) [50] at the onset of merger; i.e., the thermal energy per nucleon is much smaller than the Fermi energy of neutrons. Hence, cold nuclear EOSs are employed in giving the initial condition.

We choose binaries of an orbital separation which is slightly larger than that for an innermost orbit. Here, the innermost orbit is defined as a close orbit for which Lagrange points appear at the inner edge of at least one of two neutron stars [42, 51]. If the orbital separation

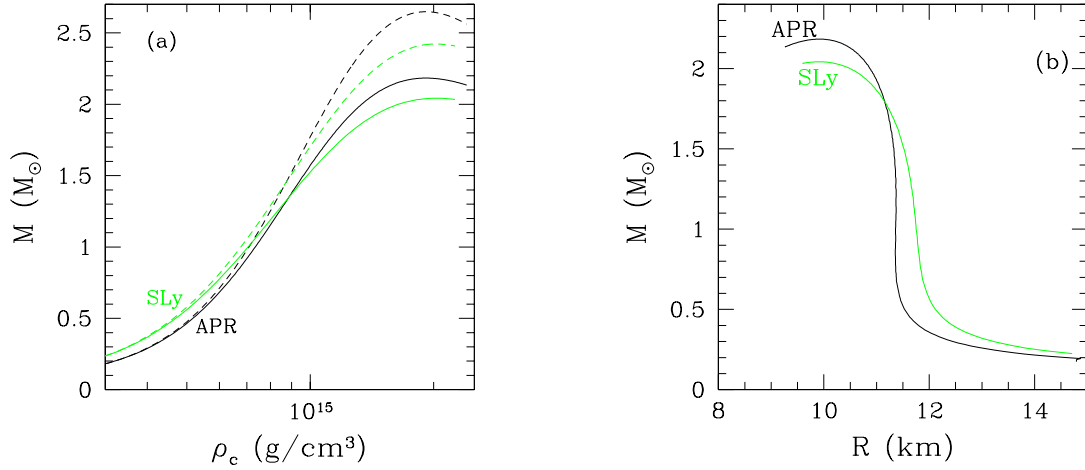


FIG. 2: (a) ADM mass (solid curves) and total baryon rest-mass (dashed curves) as a function of central baryon rest-mass density ρ_c and (b) relation between the circumferential radius and the ADM mass for cold and spherical neutron stars in equilibrium. “APR” and “SLy” denote the sequences for the APR and SLy EOSs, respectively.

Model	$M_\infty(M_\odot)$	$\rho_{\max}(10^{14}\text{g}/\text{cm}^3)$	Q_M	$M_*(M_\odot)$	$M_0(M_\odot)$	q_0	P_0 (ms)	C_0	Q_*
APR1313	1.30, 1.30	8.62, 8.62	1.00	2.858	2.568	0.918	2.064	0.114	1.075
APR1214	1.20, 1.40	8.28, 9.10	0.842	2.861	2.569	0.920	2.158	0.111	1.076
APR135135	1.35, 1.35	8.85, 8.85	1.00	2.981	2.665	0.906	1.992	0.120	1.125
APR1414	1.40, 1.40	9.09, 9.09	1.00	3.106	2.762	0.896	1.923	0.125	1.173
APR1515	1.50, 1.50	9.59, 9.56	1.00	3.360	2.957	0.879	1.838	0.135	1.269
APR145155	1.45, 1.55	9.34, 9.86	0.927	3.360	2.959	0.886	1.969	0.129	1.269
APR1416	1.40, 1.60	9.09, 10.14	0.862	3.363	2.960	0.892	1.969	0.129	1.270
APR135165	1.35, 1.65	8.85, 10.43	0.800	3.366	2.960	0.888	1.968	0.129	1.271
APR1317	1.30, 1.70	8.62, 10.74	0.743	3.370	2.960	0.883	2.057	0.126	1.272
APR125175	1.25, 1.75	8.40, 11.09	0.690	3.377	2.962	0.885	2.145	0.122	1.275
APR1218	1.20, 1.80	8.17, 11.44	0.639	3.378	2.957	0.861	2.189	0.120	1.275
SLy1313	1.30, 1.30	8.57, 8.57	1.00	2.847	2.568	0.922	2.110	0.112	1.175
SLy1414	1.40, 1.40	9.16, 9.16	1.00	3.093	2.763	0.902	2.012	0.122	1.277
SLy135145	1.35, 1.45	8.85, 9.48	0.923	3.094	2.763	0.901	2.013	0.122	1.277
SLy1315	1.30, 1.50	8.56, 9.80	0.851	3.096	2.764	0.904	2.104	0.118	1.278
SLy125155	1.25, 1.55	8.42, 10.15	0.786	3.099	2.765	0.904	2.150	0.117	1.278
SLy1216	1.20, 1.60	8.02, 10.54	0.726	3.103	2.765	0.903	2.242	0.113	1.279

TABLE II: List of several quantities for initial data (binary neutron stars in quasicircular orbits). The ADM mass of each star when they are in isolation M_∞ , the maximum density for each star, the baryon rest-mass ratio $Q_M \equiv M_{*2}/M_{*1}$, the total baryon rest-mass, the total ADM mass M_0 , non-dimensional spin parameter $q_0 = J_0/M_0^2$, orbital period P_0 , the orbital compactness [$C_0 \equiv (M_0\Omega)^{2/3}$], and the ratio of the total baryon rest-mass to the maximum allowed mass for a spherical and cold neutron star ($Q_* \equiv M_*/M_{* \max}^{\text{sph}}$).

becomes smaller than that of the innermost orbit, mass transfer sets in and a dumbbell-like structure is formed. Until the innermost orbit is reached, the circular orbit is stable, and hence, the innermost stable circular orbit (ISCO) does not exist outside the innermost orbit for the present cases. However, the ISCO seems to be close to the innermost orbit since the decrease rates of the energy and the angular momentum as a function of the orbital separation along the quasidequilibrium sequences are close

to zero near the innermost orbit.

The ADM mass of each neutron star, when it is in isolation (i.e., when the orbital separation is infinity), is denoted by M_∞ , and chosen in the range between $1.2M_\odot$ and $1.8M_\odot$. The labels APR and SLy denote the binary models constructed in the APR and SLy EOSs, respectively. We select the models for a wide range of rest-mass ratio, $0.6 \lesssim Q_M \leq 1$, to find the dependence of the disk mass around a black hole on Q_M for the high-mass case

Model	Grid size	L (km)	λ_0 (km)	f_{merger} (kHz)	λ_{merger} (km)	Product	Disk mass (M_{\odot})
APR1313	(665, 665, 333)	139	309	3.20	94	NS	—
APR1313b	(377, 377, 189)	78.7	309	3.18	94	NS	—
APR1214	(377, 377, 189)	74.5	323	3.23	93	NS	—
APR135135	(377, 377, 189)	77.8	299	3.35	89	NS	—
APR1414	(665, 665, 333)	135	288	3.79	79	NS	—
APR1515	(633, 633, 317)	125	276	6.5	46	BH	4×10^{-4}
APR1515b	(377, 377, 189)	74.5	276	—	—	BH	2×10^{-4}
APR145155	(633, 633, 317)	125	295	6.5	46	BH	5×10^{-4}
APR1416	(633, 633, 317)	125	295	6.5	46	BH	1.0×10^{-3}
APR1416b	(377, 377, 189)	74.5	295	—	—	BH	7×10^{-4}
APR135165	(633, 633, 317)	125	295	6.5	46	BH	2.7×10^{-3}
APR135165b	(377, 377, 189)	74.5	295	—	—	BH	1.9×10^{-3}
APR1317	(633, 633, 317)	125	308	6.5	46	BH	6.9×10^{-3}
APR1317b	(377, 377, 189)	74.5	308	—	—	BH	5.0×10^{-3}
APR125175	(377, 377, 189)	74.5	276	—	—	BH	1.2×10^{-2}
APR1218	(377, 377, 189)	74.5	276	—	—	BH	1.5×10^{-2}
SLy1313	(633, 633, 317)	131	316	3.20	94	NS	—
SLy1414	(633, 633, 317)	131	302	6.7	45	BH	4×10^{-3}
SLy1414b	(377, 377, 189)	77.8	302	—	—	BH	3×10^{-3}
SLy135145	(377, 377, 189)	77.8	302	—	—	BH	5×10^{-3}
SLy1315	(377, 377, 189)	77.8	315	—	—	BH	1.4×10^{-2}
SLy125155	(633, 633, 317)	131	322	6.7	45	BH	4.9×10^{-2}
SLy125155b	(377, 377, 189)	77.8	322	—	—	BH	3.6×10^{-2}
SLy1216	(377, 377, 189)	77.8	336	—	—	BH	5.7×10^{-2}

TABLE III: List of setting for simulation and summary of the outcome. L , λ_0 , and f_{merger} denote the location of outer boundaries along each axis, the wave length of gravitational waves at $t = 0$, and the frequency of gravitational waves from the formed hypermassive neutron stars or of ring-down gravitational waves of a quasinormal mode of black holes, respectively. λ_{merger} denotes the wave length of gravitational waves $\lambda_{\text{merger}} = c/f_{\text{merger}}$, which is shown to be $\lesssim L$ for the large grid sizes. In the last two columns, the product at $t = 10$ ms and disk mass for the black hole formation case are shown. “NS” implies that a hypermassive neutron star is the outcome at $t = 10$ ms, and “BH” implies that a black hole is promptly formed. The disk mass is evaluated at $t - t_{\text{AH}} = 0.5$ ms where t_{AH} is the time at apparent horizon formation. Note that we do not compute gravitational waves for the small grid size (377, 377, 189) in the case of prompt black hole formation.

with $M \sim 2.76\text{--}2.96M_{\odot}$.

The simulations are performed using a fixed uniform grid in the reflection symmetry with respect to the equatorial plane (the orbital plane). In this paper, the typical grid size is (633, 633, 317) or (665, 665, 333) for (x, y, z) . The grid covers the region $-L \leq x \leq L$, $-L \leq y \leq L$, and $0 \leq z \leq L$ where L is a constant. The grid spacing Δx is ≈ 0.4 km with which the major diameter of each star is covered with about 45 grid points initially. We have shown that with this grid spacing, a convergent numerical result is obtained in the merger simulations [17].

Accuracy in the computation of gravitational waveforms (in particular amplitude) and the radiation reaction depends on the location of the outer boundaries if the wavelength, λ , is larger than L [17]. For $L \lesssim 0.4\lambda$, the amplitude and the radiation reaction of gravitational waves are significantly overestimated [17, 52]. Due to the restriction of the computational power, it is difficult to

take a huge grid size in which L is much larger than λ . As a consequence of the present restricted computational resources, L has to be chosen as $\sim 0.4\text{--}0.45\lambda_0$ where λ_0 denotes the value of λ at $t = 0$. Hence, the error associated with the small value of L is inevitable; the amplitude and radiation reaction of gravitational waves are overestimated in the early phase of the simulation. The overestimation of the radiation reaction leads to slight spurious shortening of the late inspiraling phase.

However, the typical wavelength of gravitational waves just before the merger quickly becomes shorter due to a short radiation-reaction time scale, and hence, the accuracy of the wave extraction is improved with the evolution of the system. In particular, the wavelength of quasiperiodic gravitational waves emitted from the formed hypermassive neutron star and of ring-down gravitational waves associated with a quasinormal mode of the formed black hole (denoted by λ_{merger}) is much shorter than λ_0 and satisfies the condition $\lambda_{\text{merger}} < L$

for the grid size (633, 633, 317) (see Table III). Therefore, the waveforms in the merger stage are computed accurately (within $\sim 10\%$ error) as confirmed in [17].

For some models, the simulations are performed for a smaller grid size (377, 377, 189) but with the same grid spacing Δx . In this case, gravitational waveforms cannot be accurately computed for the inspiraling phase because of the small value of L/λ_0 . However, if we pay attention only to the outcome after the merger, such small value for L may be allowed since the properties of the outcome depend weakly on L . This fact is indeed confirmed in the simulations for several models (cf. Table III; about the reason for the systematic underestimation of the disk mass, see IVC 1). Thus, we perform simulations for models APR135135, APR1214, APR125175, APR1218, SLy135145, SLy1315, and SLy1216 only with the small grid size. In this case, the focus is only on the outcome, not on computing gravitational waveforms.

With the (633, 633, 317) grid size, about 240 GBytes computational memory is required. For the case of the hypermassive neutron star formation, the simulations are performed for about 30,000 time steps (until $t \sim 10$ ms) and then stopped to save the computational time. The computational time for one model in such a simulation is about 180 CPU hours using 32 processors on FACOM VPP5000 in the data processing center of National Astronomical Observatory of Japan (NAOJ). For the case of the black hole formation, the simulations are continued until mass accretion rate from the surrounding disk to a formed black hole relaxes approximately to a constant. In this case, the computational time is about 60 CPU hours for about 12,000 time steps.

IV. NUMERICAL RESULTS: MERGER PROCESS

A. Summary of the outcome

For all the cases, the binary orbit is stable at $t = 0$, but after slight decrease of the orbital separation due to gravitational radiation reaction, merger sets in. In the present simulations, the merger starts in one orbit (in $t \sim 2$ ms) irrespective of the models. If the total ADM mass of the system is high enough, a black hole is formed within ~ 1 ms after two stars come into contact. On the other hand, for models with the ADM mass smaller than a threshold mass M_{thr} , a hypermassive neutron star is formed and survives for more than 10 ms. However, it will collapse to a black hole eventually due to gravitational radiation reaction or angular momentum transport by other effects (see discussion in Sec. IV B 3). In the case of black hole formation (models APR1515, APR1416, APR135165, APR1317, APR125175, APR1218, SLy1414, SLy135145, SLy1315, SLy125155, and SLy1216), the evolution of the black holes is followed using a black hole excision technique [29] until the mass accretion rate from the disk to the

formed black hole becomes approximately constant.

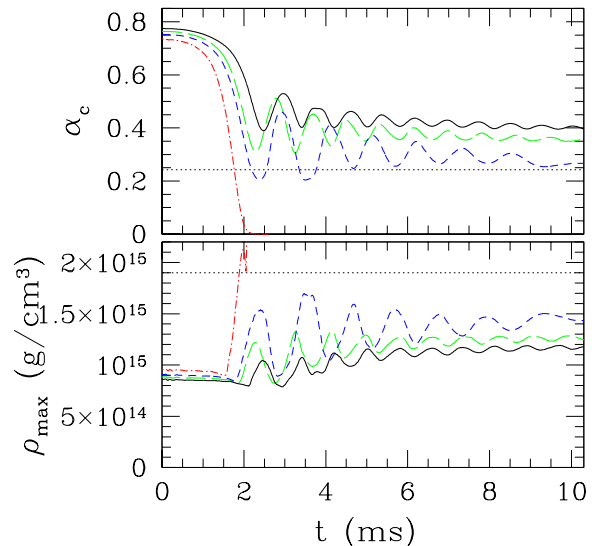


FIG. 3: Evolution of the central value of the lapse function α_c and the maximum values of the rest-mass density ρ_{max} for models APR1313 (solid curves), APR135135 (long-dashed curves), APR1414 (dashed curves), and APR1515 (dot-dashed curves). The dotted horizontal lines denote the central values of the lapse and rest-mass density for the marginally-stable, spherical neutron star in equilibrium with the cold APR EOS.

In Fig. 3, we show the evolution of the central value of the lapse function α_c and the maximum of the baryon rest-mass density ρ_{max} for models APR1313, APR135135, APR1414, and APR1515. For model APR1515, α_c collapses to zero and ρ_{max} quickly increases at $t \sim 1.5$ ms, implying that a black hole is formed promptly soon after the onset of the merger (at $t \approx 2.04$ ms). For other cases, α_c and ρ_{max} settle down to relaxed values, implying that a quasistationary neutron star is formed. Since the mass is larger than the maximum allowed limit of rigidly rotating neutron stars, these neutron stars are hypermassive [23].

For model APR1414, α_c and ρ_{max} oscillate with an amplitude larger than that for models APR1313 and APR135135. This behavior results from the fact that the self-gravity is large enough for the merged object to deeply shrink surmounting the centrifugal force. This indicates that the total ADM mass of this model ($M \approx 2.76M_\odot$) is slightly smaller than the threshold value for the prompt black hole formation. Since a black hole is formed for $M \approx 2.96M_\odot$, the threshold mass for black hole formation is $M_{\text{thr}} \approx 2.8\text{--}2.9M_\odot$. In a previous paper [21], we adopted the SLy and FPS (Friedman-Pandharipande-Skyrme) EOSs and found that $M_{\text{thr}} \approx 2.7M_\odot$ and $2.5M_\odot$, respectively. The high value of M_{thr} for the APR EOS is reasonable since it is stiffer than the SLy and FPS EOSs, and the maximum allowed mass for spherical, cold neutron star M_{sph} is also larger. The present result combined with the previous one [21] suggests an empirical relation $M_{\text{thr}}/M_{\text{sph}} = 1.30\text{--}1.35$ for

these stiff nuclear EOSs.

We note that this relation is highly different from that for the Γ -law EOS with $\Gamma = 2$ [17] for which $M_{\text{thr}}/M_{\text{sph}} \approx 1.7$. As discussed in [21], the compactness of each neutron star in the stiff nuclear EOSs is larger than that with the $\Gamma = 2$ EOS for a given mass. Accordingly, for a given total mass, the binary system at the onset of the merger is more compact. This implies that the angular momentum is dissipated more before the merger sets in with the stiff nuclear EOSs. The dissipation of the angular momentum by $\sim 0.1J_0$ before the merger helps the prompt black hole formation, since the hypermassive neutron star formation requires a substantial centrifugal force to sustain the self-gravity.

In recent papers [53], ratio of the maximum mass of hypermassive neutron stars in equilibrium to M_{sph} has been investigated in detail. These works coincidentally show a similar dependence of the ratio $M_{\text{thr}}/M_{\text{sph}}$ on the EOSs. Hence, the small value of $M_{\text{thr}}/M_{\text{sph}}$ may be partly due to the absence of high-mass differentially rotating neutron stars in equilibrium.

In Figs. 4–8, we display the snapshots of the density contour curves and the velocity vectors in the equatorial plane at selected time slices for models APR1313, APR1414, APR1515, APR1416, and APR1317, respectively. In the first two cases, a hypermassive neutron star is formed, while a black hole is a prompt outcome in other three cases. For models APR1515, APR1416, and APR1317, the ADM mass of the system is approximately identical while the mass ratio is different. The structure and density of disk surrounding the formed black hole depend significantly on the mass ratio as found from Figs. 6–8. Figure 9 displays the density contour curves and the velocity vectors in the $y = 0$ plane for models APR1313, APR1414, APR1515, APR1416, APR135165, and APR1317 at a late time when the mass accretion rate relaxes approximately to a constant. This shows that (i) the hypermassive neutron stars have a highly flattened structure and (ii) the disk surrounding the black hole is geometrically thin for the mass ratio close to unity but can be thick for the smaller mass ratios with $Q_M \lesssim 0.8$.

Figure 10 shows the angular velocity along the x and y axes (a) of relaxed hypermassive neutron stars for models APR1313 and APR1414 and (b) of the disk surrounding the black hole for model APR135165. This illustrates that the hypermassive neutron stars, in particular in their outer region, are differentially rotating and the central part is rapidly rotating with the rotational period shorter than 1 ms. The disk surrounding the black hole has approximately a Kepler orbit outside the ISCO (for which the estimated coordinate radius is ~ 10 km).

In the following two subsections, details about the formation process of hypermassive neutron stars and black holes are discussed separately. Implication of the results to formation of a central engine of SGRBs is also discussed in the subsequent section IV D.

B. Formation of hypermassive neutron star

1. Models APR1313 and APR135135

In the formation of the hypermassive neutron stars from equal-mass neutron stars with relatively low total mass $\sim 2.6\text{--}2.7M_\odot$ (models APR1313 and APR135135), a double core structure is first formed (see the snapshot at $t = 3.218$ ms of Fig. 4), and then, it relaxes to a highly nonaxisymmetric ellipsoid [see the snapshots for $t > 4$ ms of Fig. 4 and 9(a)]. The contour plots, drawn for a high-density region with the rest-mass density larger than the nuclear density $\sim 2 \times 10^{14}$ g/cm³, show that the axial ratio of the ellipsoid measured in the equatorial plane is $\lesssim 0.8$ for $t \gtrsim 4$ ms. Figure 9(a) also shows that the axial length along the z -axis for $\rho \geq 2 \times 10^{14}$ g/cm³ is about 7 km, which is $\sim 70\%$ of the major axis. Namely, a rotating ellipsoid of a large ellipticity is the outcome. This result is essentially the same as that found in [21] for models SLy1313 and SLy125135. This large ellipticity is achieved due to the rapid rotation and the high stiffness of the chosen EOS.

The rapid rotation is found from Fig. 10(a); it shows that the rotational period of the central region is shorter than 1 ms at $t \sim 10$ ms, at which the hypermassive neutron star relaxes approximately to a stationary state. This indicates that the rotational centrifugal force plays an important role for sustaining the large self-gravity of the hypermassive neutron stars [23, 54].

For the unequal-mass case with $Q_M \approx 0.85$ (model APR1214), the smaller-mass neutron star is tidally elongated at the merger. As a result, the double-core structure is not formed in contrast to model APR1313. However, the formed hypermassive neutron star relaxes to an ellipsoid in the similar way to model APR1313. Subsequent evolution proceeds in essentially the same manner to that in the equal-mass case.

The merger for model APR135135 proceeds in qualitatively the same way as that for model APR1313. Quantitatively, the results such as the ellipticity and the rotational period of the hypermassive neutron star are slightly different reflecting the difference in the mass; ellipticity is slightly smaller and the rotational period is slightly shorter because of its larger compactness.

Because of the nonaxisymmetric structure, the hypermassive neutron stars found for models APR1313, APR1214, and APR135135 emit quasiperiodic gravitational waves and the angular momentum is dissipated substantially. However, the dissipation time scale is much longer than 10 ms, implying that they remain the ellipsoidal star for longer than 10 ms (cf. Sec. V). These ellipsoids are also differentially rotating (cf. Fig. 10). Thus, they are subject to angular momentum transport by magnetic effects [23, 55, 56, 57]. However, note that the time scale of the angular momentum transport is shorter than ~ 100 ms only when very strong magnetic fields greater than $\sim 10^{15}$ G are present [23].

Assume that the dissipation time scale by gravitational

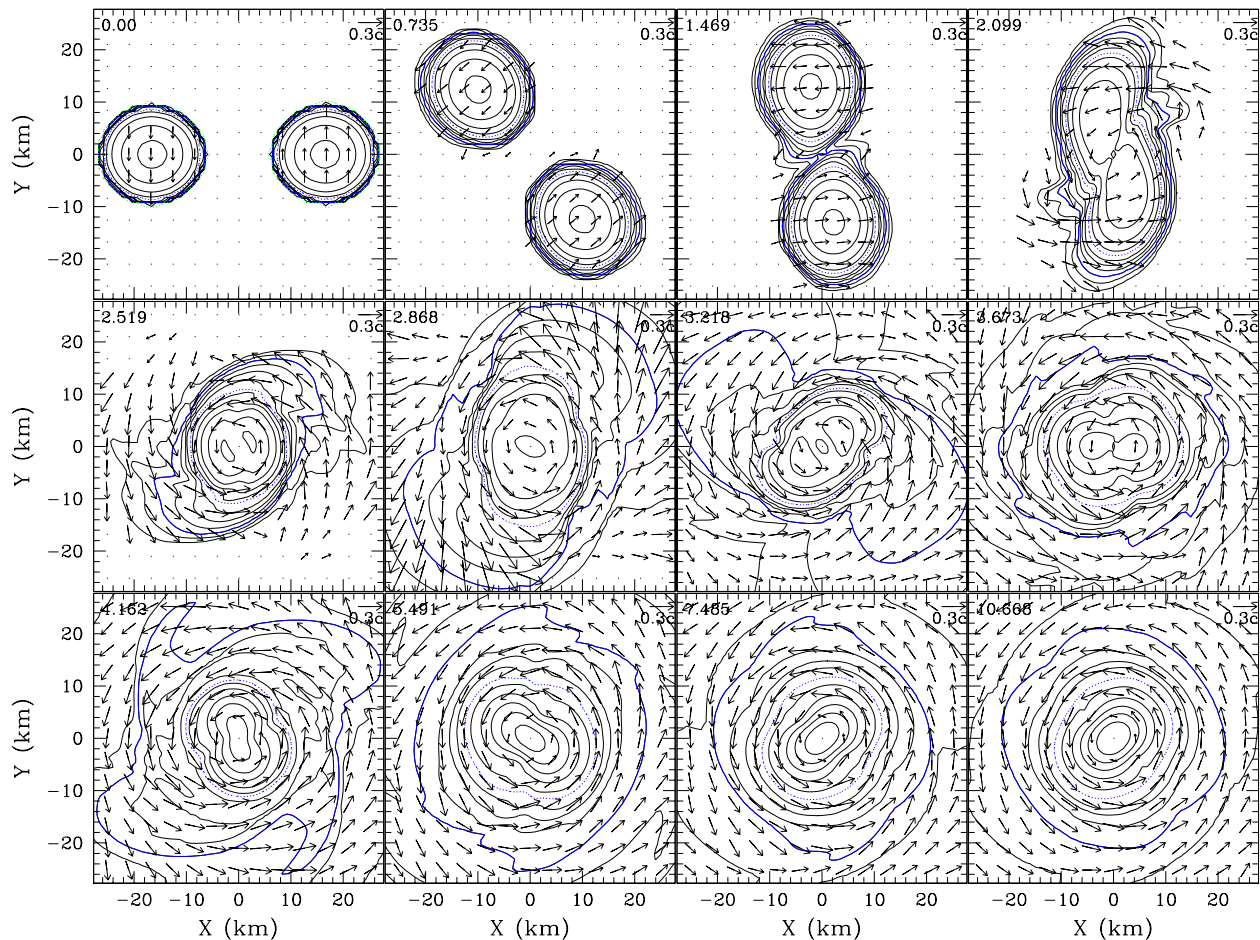


FIG. 4: Snapshots of the density contour curves for ρ in the equatorial plane for model APR1313. The solid contour curves are drawn for $\rho = 2 \times 10^{14} \times i \text{ g/cm}^3$ ($i = 1, 2, 3, \dots$) and for $1 \times 10^{14-0.5i} \text{ g/cm}^3$ ($i = 1 \sim 6$). The (blue) thick dotted and solid curves denote $1 \times 10^{14} \text{ g/cm}^3$ and $1 \times 10^{12} \text{ g/cm}^3$, respectively. The number in the upper left-hand side denotes the elapsed time from the beginning of the simulation in units of ms. Vectors indicate the local velocity field (v^x, v^y), and the scale is shown in the upper right-hand corner.

waves is shortest among other processes. Then, there are two possible fates after a longterm emission of gravitational waves. One fate is that after the angular momentum dissipation, the centrifugal force becomes weak enough to induce gravitational collapse to a black hole. The other is that the angular momentum (i.e., rotational kinetic energy) is dissipated to be too small to maintain the nonaxisymmetric structure and, consequently, a spheroidal star in a stationary state is formed. (It is well known that an elliptical structure can be achieved only in the case that the ratio of the rotational kinetic energy to the gravitational binding energy is large enough [58].) If the time scale for the decrease of the angular momentum is shorter (longer) than that for the decrease of the ellipticity, a black hole (a spheroidal hypermassive neutron star) is the outcome. In the formation of a spheroid, subsequent evolution will be determined by other processes such as angular momentum transport by

the magnetic braking [23] or the magnetorotational instability (MRI) [55]. In the previous paper [21] in which the SLy and FPS EOSs are adopted, we have found that a black hole is the outcome (see the results for models SLy135135b and FPS125125b in [21]). As the merger process depends weakly on the EOSs, the black hole formation may be also the fate in the APR EOS. However, this may not hold as illustrated in the next section for high-mass model APR1414. To answer this question, an extremely longterm simulation up to $t \sim 100$ ms is necessary. This problem is left as the future issue.

2. Model APR1414

In the formation of the hypermassive neutron stars with high mass $\sim 2.8M_{\odot}$ (model APR1414), the evolution proceeds in a different manner from that for models

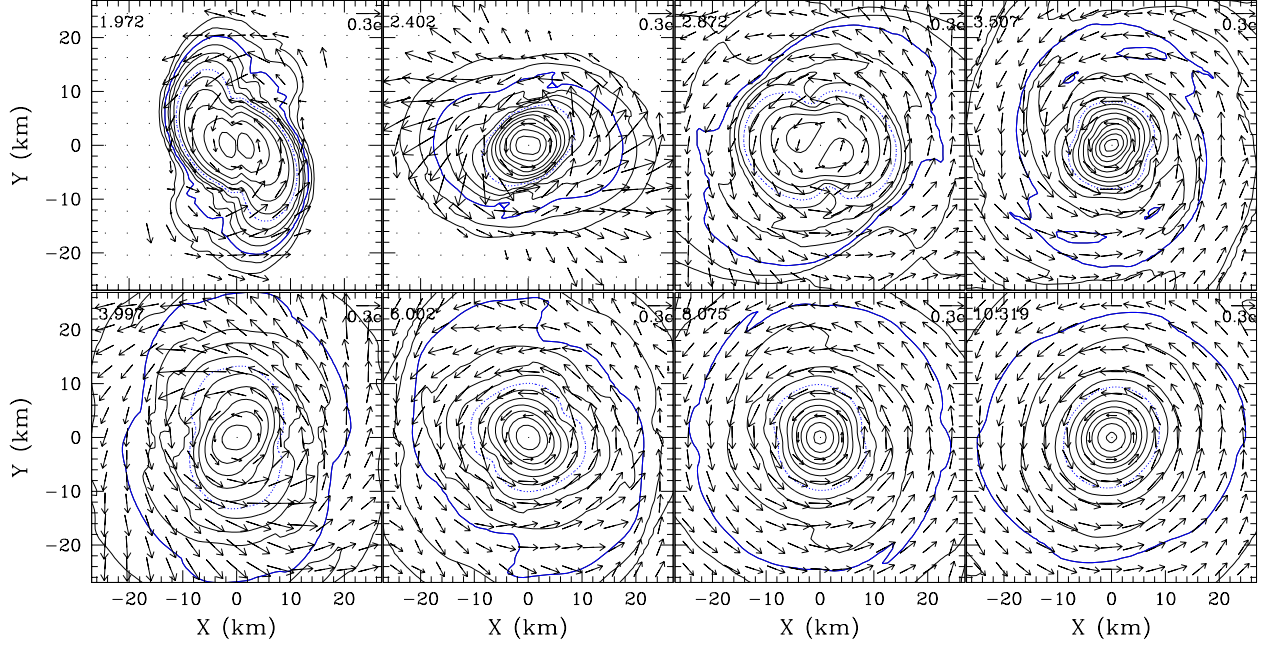
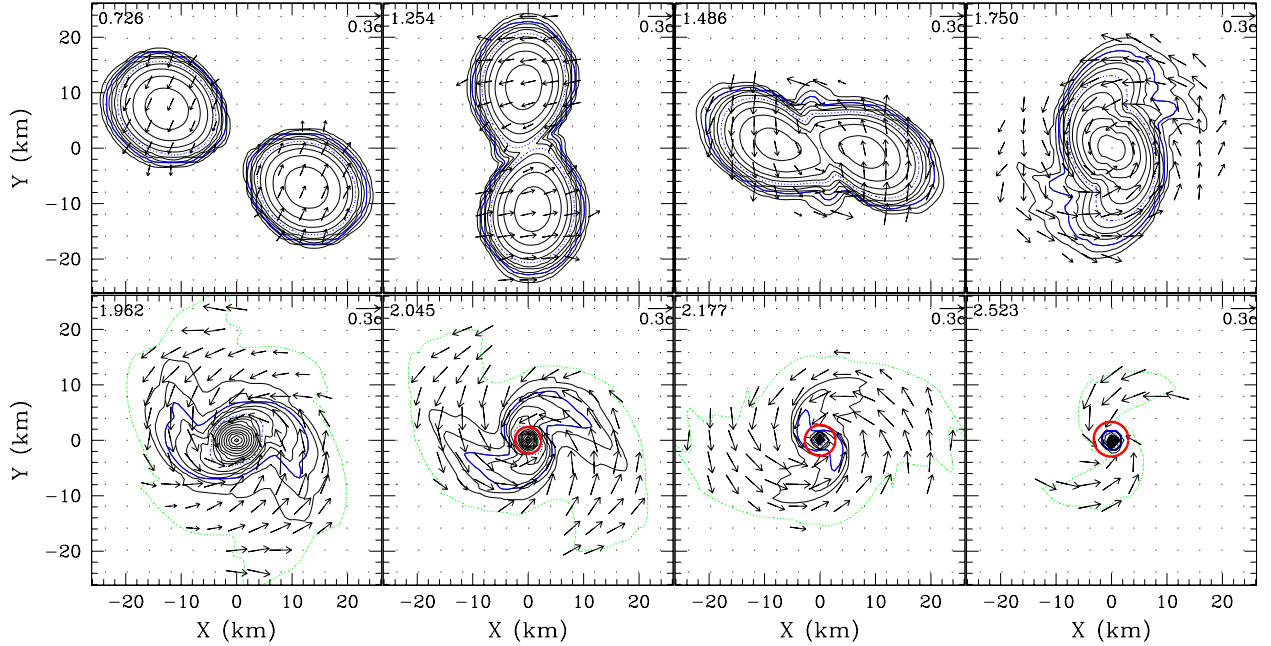


FIG. 5: The same as Fig. 4 but for model APR1414.

FIG. 6: The same as Fig. 4 but for model APR1515. The outermost (green) dotted curves denote $1 \times 10^{10} \text{ g/cm}^3$. The thick circles around the origin in the last three panels denote the location of the apparent horizon.

APR1313 and APR135135. Since the mass is larger, a more compact merged object is formed soon after the onset of the merger (second panel of Fig. 5). Then, it bounces back to a state with a large radius (or a small density; cf. Fig. 3) and repeats quasiradial oscillations with a large amplitude before relaxing to a hypermas-

sive neutron star in a quasistationary state. At the state of the large radius, the angular momentum is efficiently transported from the inner region to the outer envelop (see discussion below). On the other hand, the compact state achieved at maximum compressions (cf. second and fourth panels of Fig. 5) results in a large amount of angu-

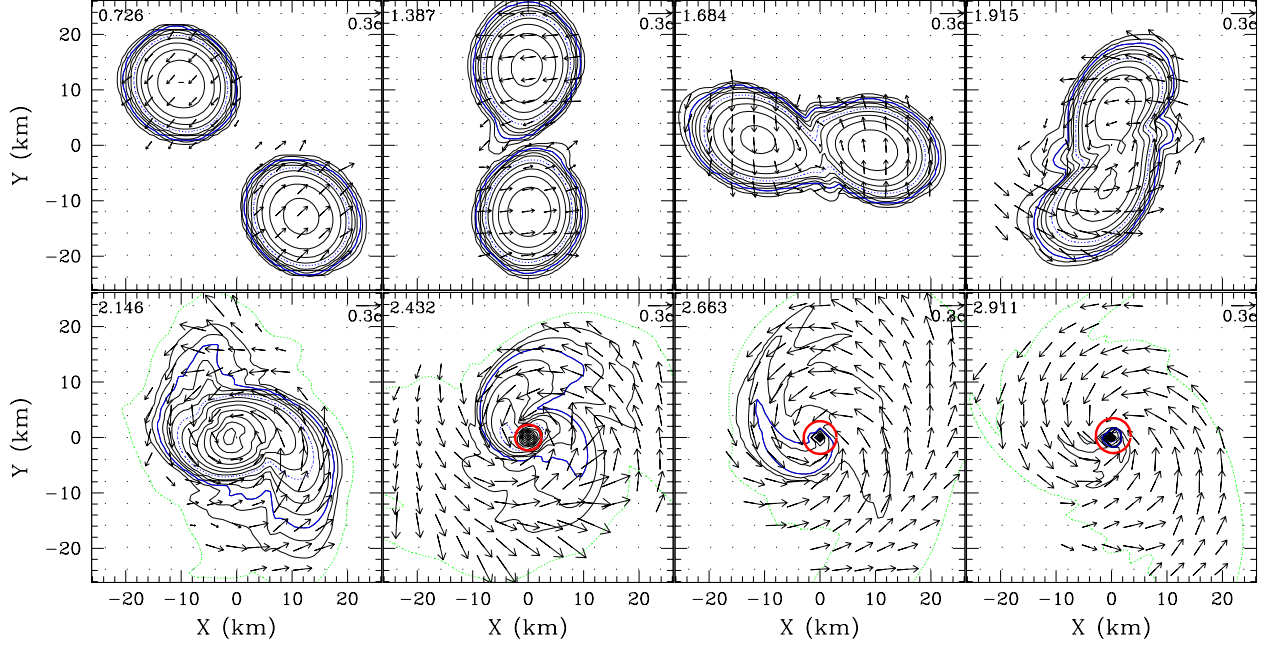


FIG. 7: The same as Fig. 6 but for model APR1416.

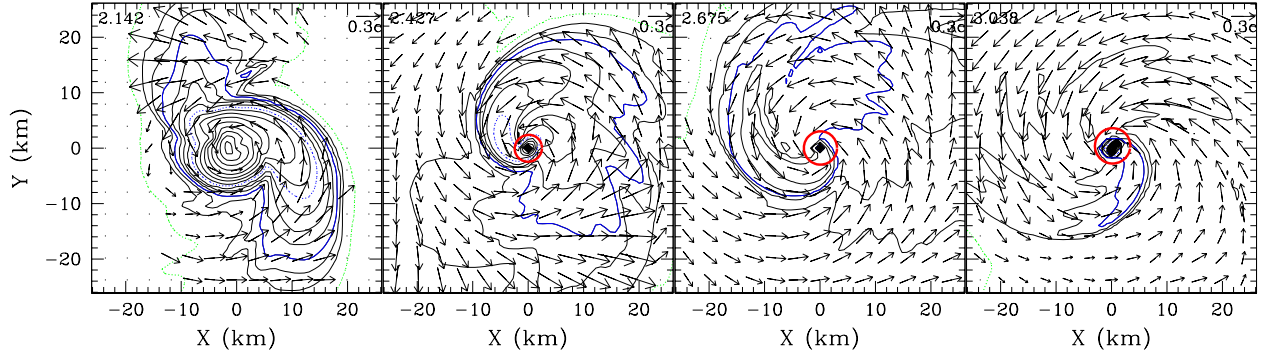


FIG. 8: The same as Fig. 6 but for model APR1317.

lar momentum dissipation via gravitational radiation (cf. Sec V). These effects subsequently lead the hypermassive neutron star to a state with relatively small angular momentum.

The decrease of the angular momentum in a shorter time results in a state of small rotational kinetic energy. On the other hand, the gravitational binding energy is larger than in models APR1313 and APR135135, because of its larger compactness. As mentioned in the last part of Sec. IV B 1, an elliptical structure can be achieved only in the case that the ratio of the rotational kinetic energy to the gravitational binding energy is large enough [58]. For the hypermassive neutron star formed in model APR1414, this ratio should be smaller than those in models APR1313 and APR135135. Consequently, a spheroid of small ellipticity is formed [cf. the last three

panels of Fig. 5 and 9(b)]. This results in the facts that luminosity of gravitational waves is much smaller than for model APR1313 for $t \gtrsim 5$ ms (cf. Sec. V), and the dissipation time scale of the angular momentum by gravitational radiation is much longer. In model APR1414, probably, dissipation by gravitational radiation will not induce gravitational collapse.

As in the hypermassive neutron star for model APR1313, the outer region with the coordinate radius $R \gtrsim 8$ km is differentially rotating [see Fig. 10(a)]. Such differentially rotating region is subject to the magnetic braking and the MRI in the presence of magnetic fields [55, 56, 57]. If the instabilities turn on, the magnetic fields play an important role for transporting angular momentum outward, subtracting the angular momentum of the central part. Hence, a plausible scenario for the

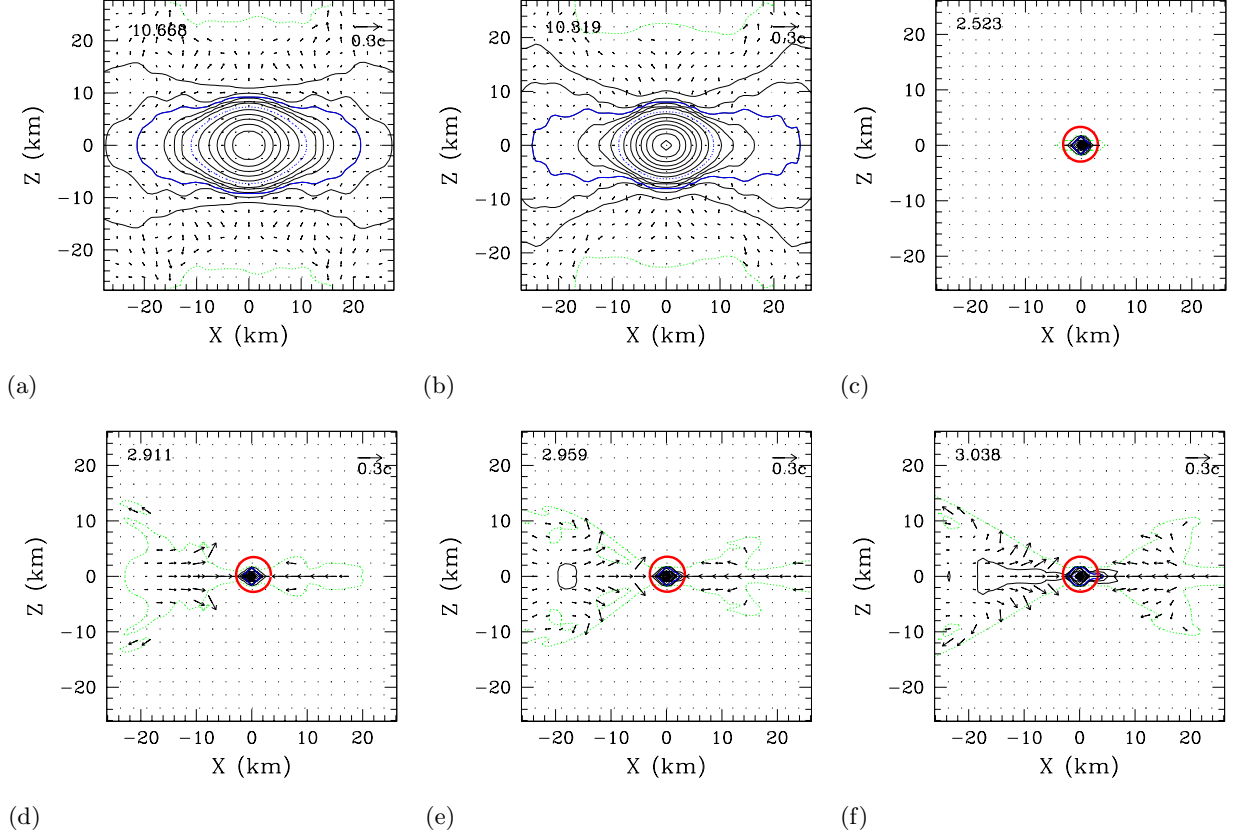


FIG. 9: The density contour curves for ρ and the local velocity field (v^x, v^z) in the $y = 0$ plane (a) at $t = 10.668$ ms for model APR1313, (b) at $t = 10.319$ ms for APR1414, (c) at $t = 2.523$ ms for APR1515, (d) at $t = 2.911$ ms for APR1416, (e) at $t = 2.959$ ms for APR135165, and (f) at $t = 3.038$ ms for APR1317. The contour curves and the velocity vectors are drawn in the same way as in Fig. 6.

hypermassive neutron star of model APR1414 is the collapse to a black hole by the magnetic effects.

Finally, we note that in the previous paper [21] in which the SLy and FPS EOSs are used, we have not found the formation of spheroids, but rather, gravitational radiation triggers the collapse of hypermassive neutron stars to a black hole. The likely reason in this difference is that the APR EOS is stiffer than others. Namely, the hypermassive neutron stars can be more compact with this EOS [cf. Fig. 2(b)] escaping the collapse. In such extremely compact state, the gravitational binding energy would be large enough to reduce the ratio of the rotational kinetic energy to the binding energy below the threshold value of the formation of an ellipsoid.

3. Angular momentum transport and disk mass

Due to a torque by the nonaxisymmetric structure of the merged object, angular momentum is transported from the inner region to the outer one. As a result, the rotational angular velocity $\Omega = v^\varphi$ near the center decreases and its profile is modified. Figure 10 shows the angular velocity Ω of the hypermassive neutron stars

along x and y axes at $t \gtrsim 10$ ms. The hypermassive neutron stars are differentially and rapidly rotating at the birth [21]; the rotational period around the central region is ≈ 0.2 – 0.3 ms at the birth. (The rotational period of the double core found in Figs. 4 and 5, which is formed soon after the merger, is ~ 0.2 – 0.3 ms. This is found from the frequency of gravitational waves; cf. Sec. V). The angular momentum is then redistributed by the torque, resulting in a fairly uniform profile of Ω near the rotational axis with $R \lesssim 8$ km.

The significance of the angular momentum transport is also found from the evolution of the mass spectrum as a function of the specific angular momentum, $M_*(j)$. Here, the specific angular momentum j is defined by hu_φ and the mass spectrum $M_*(j_0)$ is given by an integrated baryon rest-mass of fluid elements with $j \leq j_0$;

$$M_*(j_0) = \int_{j < j_0} \rho_* d^3x. \quad (28)$$

In Fig. 11, we show this mass spectrum at selected time slices for models APR1313 and APR1414. This illustrates that the fraction of baryon rest-mass with $j \gtrsim 1.4M_0$ is absent at $t = 0$ but increases with time. This is due to the angular momentum transport from the

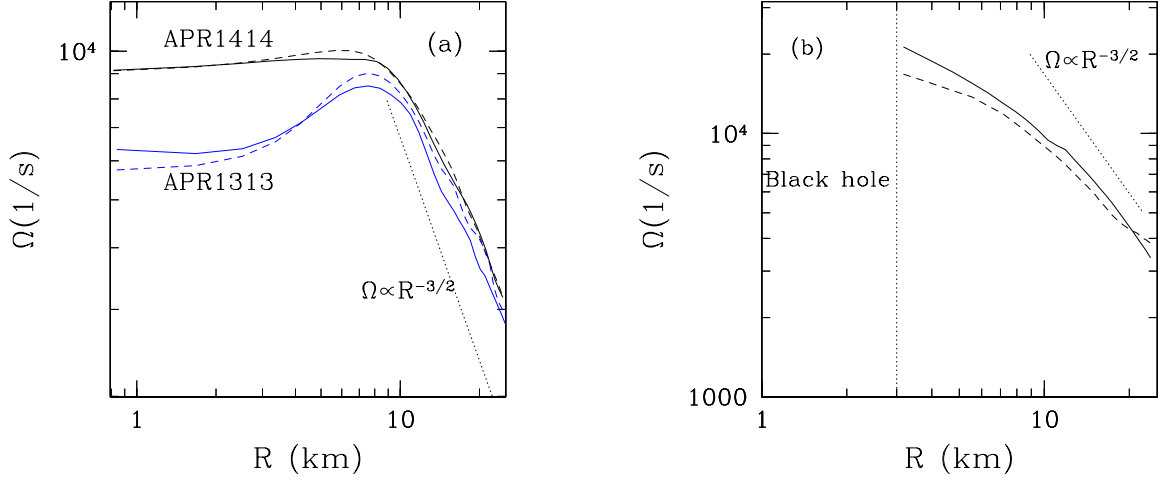


FIG. 10: (a) The angular velocity Ω of hypermassive neutron stars along x (solid curves) and y axes (dashed curves) for model APR1313 (blue) at $t = 10.668$ ms and for APR1414 (black) at $t = 10.319$ ms. (b) Ω of accretion disk around a central black hole for model APR135165 along x (solid curve) and y (dashed curve) axes at $t = 2.959$ ms. The apparent horizon is located at $r \approx 3$ km. For both figures, the horizontal axis denote the coordinate radius.

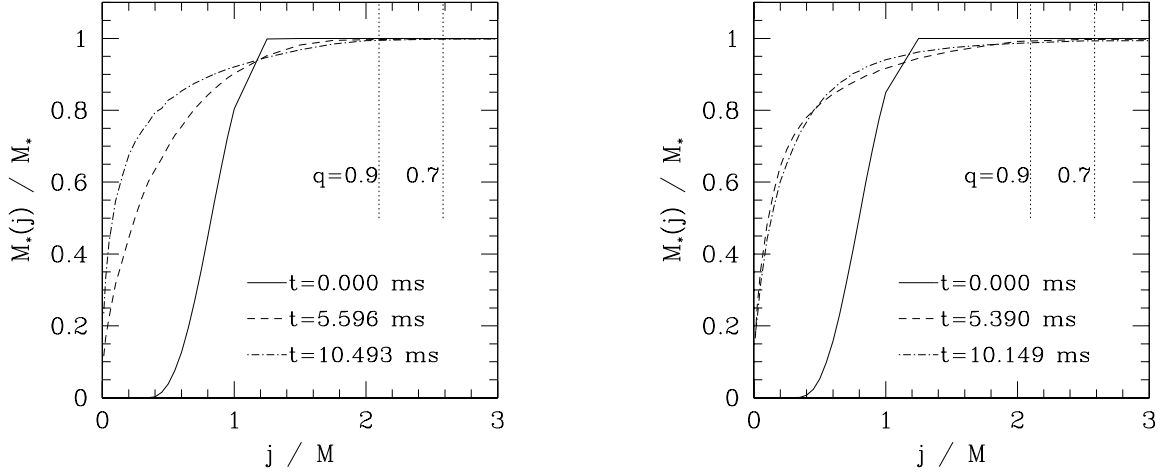


FIG. 11: Evolution of $M_*(j)$ for models APR1313 (left) and APR1414 (right). The dotted vertical lines labeled $q = 0.9$ and 0.7 denote the values of j/M at ISCOs around a Kerr black hole of the spin parameter q .

central hypermassive neutron star of ellipsoidal shape to fluid elements in the outer envelop by the torque associated with the nonaxisymmetric structure. However, the fraction of the rest-mass with $j > 2M_0$ is still $\sim 1\%$ of the total mass because such fluid elements are absent initially, and also probably because of gravitational radiation which carries away the angular momentum by $\sim 30\%$ in 10 ms (cf. Sec. V).

Assume a hypothetical case in which the central region collapses to form a black hole at $t \approx 10$ ms. Then, the ADM mass and the angular momentum of the black hole will be $\approx 0.97M_0$ and $\approx 0.7J_0$, respectively, implying that the spin parameter is $q \sim 0.7$ (cf. Sec. V). The specific angular momentum at the ISCO, j_{isco} , around a black hole with $q = 0.7$ is $\approx 2.58M$ [59] as plotted by the dotted vertical line in Fig. 11. The mass of the fluid

elements with $j \geq 2.5M$ is $\approx 0.01M_\odot$ at $t = 10$ ms for model APR1313. Namely, a disk of mass $\sim 0.01M_\odot$ will be formed in this hypothesis. The value for the disk mass is approximately identical with that presented in [31] in which a similar nuclear EOS [32] is adopted.

We note that the lifetime of the hypermassive neutron star is in reality much longer than 10 ms (assuming no other strong dissipation process than gravitational radiation), and hence, the angular momentum will be dissipated much more by gravitational radiation before formation of a black hole. Therefore, the value of q will be smaller and j_{isco} could be larger (e.g., for $q = 0.5$, $j_{\text{isco}} \approx 2.90M$). This effect will slightly reduce the disk mass. On the other hand, the angular momentum will be gradually transported in the outer region with time due to the torque from the central region of a nonaxisym-

metric shape. This effect will slightly increase the disk mass.

For model APR1414, the fraction of the rest-mass with $j \geq 2.5M$ is slightly larger as $\approx 0.02M_\odot$ at $t \approx 10$ ms. The reason is that in this case, the merged object quasiradially oscillates with a larger amplitude soon after the onset of the merger (cf. Fig. 3). During the high-amplitude oscillation, matter in the outer region expands to a large radius and can gain a torque from the ellipsoidal hypermassive neutron star for a longer time. Actually, the fraction of the rest-mass with $j \geq 2.5M$ steeply increases for $4 \text{ ms} \lesssim t \lesssim 6 \text{ ms}$ during which the hypermassive neutron star repeats quasiradial oscillations of the high amplitude. The high-amplitude oscillation results from the fact that the ADM mass of the system is close to M_{thr} . Hence, for the system of $M \lesssim M_{\text{thr}}$, the angular momentum transport efficiently works.

The outcome for model APR1414 at $t \approx 10$ ms is a hypermassive neutron star of nearly spheroidal shape. This implies that the angular momentum will not be significantly dissipated any longer and also outward angular momentum transport will not work efficiently for $t > 10$ ms. Therefore, in this case, the disk of mass at least $\approx 0.02M_\odot$ will be formed if the hypermassive neutron star collapses to a black hole by other mechanisms.

For model APR1214, for which the ADM mass is approximately identical with that for model APR1313, the less massive star is tidally elongated by the primary at the merger and subsequently forms an accretion disk around a formed hypermassive neutron star (evolution of the contour curves is similar to those of model APR1416 for $t \lesssim 2$ ms; cf. Fig. 7). Because of the nonaxisymmetric density profile, the angular momentum is transported outward more efficiently than in model APR1313. However, the baryon rest-mass with $j > 2.5M$ for model APR1214 at $t = 10$ ms is $\approx 0.025M_\odot$ which is only slightly larger than that for model APR1313, and hence, the degree of the increase is not as drastic as that reported in [31] for $Q_M \sim 0.85$. The likely reasons for our small mass are (i) the radius of neutron stars depends very weakly on each ADM mass in the APR EOS (cf. Fig. 2) and (ii) gravitational radiation carries a large amount of angular momentum (cf. Sec. V) which is not taken into account in the work of [31]. Because of the weak dependence of the stellar radius on the mass, the tidal deformation becomes important only for close orbits. At such small orbital radius, the angular momentum is already dissipated by gravitational radiation to be small, and hence, the angular momentum transport by a torque associated with the nonaxisymmetric structure does not help sufficiently increasing the mass with a large value of j .

Formation of hypermassive neutron stars from binaries of small values of $Q_M \lesssim 0.8$ is unlikely since the low-mass binary neutron star with such small value of Q_M would be absent; i.e., the mass of neutron stars should be larger than $\sim 1.2M_\odot$ while the total mass has to be smaller than M_{thr} , implying that Q_M should be larger

than ~ 0.8 . Therefore, the fraction of the mass with $j \gtrsim 2.5M$ will be at most $\sim 0.03M_\odot \approx 0.01M_*$ for the hypermassive neutron star formation case in the APR EOS.

For model SLy1313 in which a hypermassive neutron star is also formed, the merger process and subsequent evolution of the hypermassive neutron star is quite similar to those for models APR1313 and APR135135 [21]. As a consequence, the rest-mass with $j > 2.5M$ at $t = 10$ ms is the similar value $\sim 0.02M_\odot$. This suggests that the value of the disk mass depends weakly on the EOS. However, we note that the disk mass could be larger if we employ EOSs with which the neutron star radius is larger than that of the APR and SLy EOSs, and hence, the gravitational radiation reaction at the merger is less important.

Before closing this section, we note that the discussion about the disk mass here is based on the assumption that angular momentum is transported only by a torque in the hypermassive neutron stars. In the presence of magnetic fields with a sufficient strength, the angular momentum could be transported efficiently in a short time scale [56, 57], and as a result, the hypermassive neutron stars such as formed for models APR1313, APR1414, APR1214, and SLy1313 may collapse ejecting a large amount of the mass to form a disk. The system eventually formed could be composed of a black hole and a massive disk of $\gtrsim 0.05M_\odot$ as illustrated in the recent magnetohydrodynamic simulations [56, 57].

C. Formation of black hole

For binary neutron stars with $M \approx 2.96M_\odot$ in the APR EOS and $M \approx 2.76M_\odot$ in the SLy EOS, a black hole is formed soon after the onset of the merger irrespective of the mass ratio Q_M . Until two stars come into contact, evolution proceeds in the similar manner to that in the formation of hypermassive neutron stars. However, after the contact, the merged objects quickly collapse to a black hole. For the unequal-mass case, a less massive star is tidally deformed just before the merger. The degree of the deformation as well as lag angle, which is defined to be the angle in the equatorial plane between the major axis of each star and the axis connecting the centers of mass of two stars, are larger for smaller values of Q_M . Because of the nonzero lag angle, angular momentum is transported outward by a torque from the nonaxisymmetric merged object, increasing the specific angular momentum of the matter located in the outer region. Only in the case that the angular momentum transport works efficiently, an accretion disk may be formed around the central black hole since the specific angular momentum before the onset of the merger is too small as illustrated in Sec. IV B 3 (see also a discussion below).

1. Disk mass around the central black hole

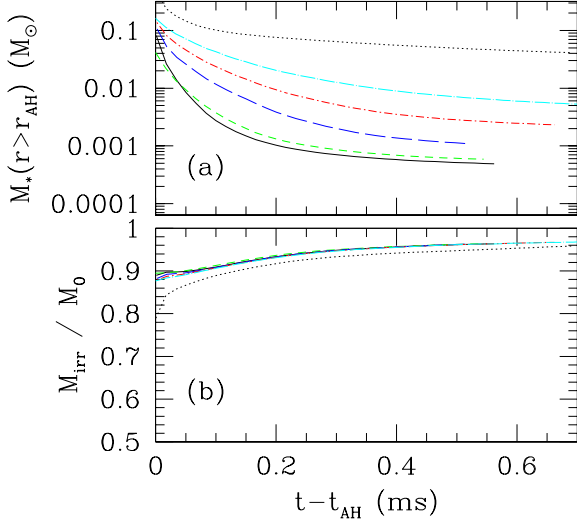


FIG. 12: (a) Evolution of the baryon rest-mass of disks surrounding black holes and (b) the evolution of irreducible mass of black holes for models APR1515 (solid curve), APR145155 (dashed curve), APR1416 (long-dashed curve), APR135165 (dot-dashed curve), APR1317 (dot-long-dashed curve), and SLy125155 (dotted curve). t_{AH} denotes the time at the first formation of an apparent horizon.

In Fig. 12(a), we plot the total baryon rest-mass located outside the apparent horizon for models APR1515, APR145155, APR1416, APR135165, APR1317, and SLy125155 as a function of $t - t_{\text{AH}}$ where t_{AH} denotes the time at the first formation of an apparent horizon. In Fig. 13, the baryon rest-mass at $t - t_{\text{AH}} = 0.5$ ms as a function of Q_M is also plotted for all the models in which a black hole is formed. These figures show that the final state is composed of a central black hole and a disk of a small mass. A rapid accretion proceeds in the first ~ 0.2 ms after formation of apparent horizon. In particular, for $Q_M \gtrsim 0.9$, most of the fluid elements are swallowed into the black hole in such a short time. With decreasing the value of Q_M , the fraction of the fluid elements which escape falling into the black hole steeply increases.

We note that for the smaller grid size, the disk mass is smaller even for the same model (cf. Table III). As mentioned in Sec. III, the inspiral time is spuriously shorten with the smaller grid size since the radiation reaction is overestimated due to the situation with $L \ll \lambda_0$. As a result, the time for transporting angular momentum outward is shorten, resulting in the decrease of the disk mass.

For $Q_M \gtrsim 0.9$, the baryon rest-mass of the disk becomes smaller than $0.01M_\odot$ within ~ 0.3 ms after formation of apparent horizon ($\approx 5 \times 10^{-4}M_\odot$ for models APR1515 and APR145155, and $\approx 5 \times 10^{-3}M_\odot$ for models SLy1414 and SLy135145). The fundamental reason is that the specific angular momentum j for all the fluid

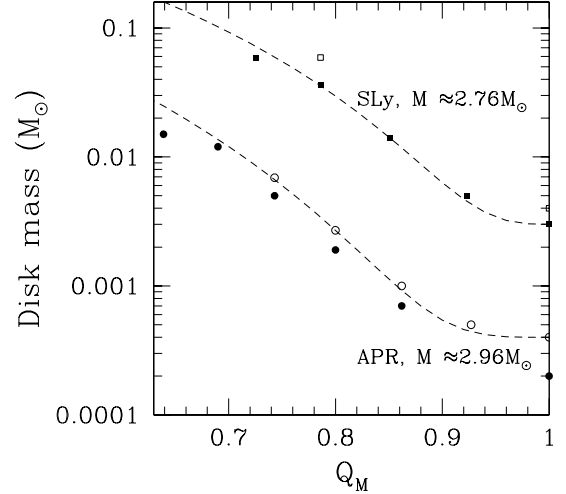


FIG. 13: Baryon rest-mass of disks around a black hole as a function of $Q_M = M_{*2}/M_{*1}$ for the black hole formation cases. The disk mass is evaluated at $t - t_{\text{AH}} = 0.5$ ms. The open circles and squares denote the results with $(633, 633, 317)$ grid size in the APR and SLy EOSs, respectively. The filled circles and squares denote the results with $(377, 377, 189)$ grid size in the APR and SLy EOSs. The dashed curves denote the fitting formulae (29). The results for the APR and SLy EOSs are derived for $M \approx 2.96M_\odot$ and $2.76M_\odot$, respectively.

elements before the merger is too small. In the present case, the maximum value of j in the initial conditions is $\sim 1.3M$, which is much smaller than the value of j at the ISCO of a Kerr black hole of mass M and spin parameter 0.7–0.9. Moreover, the specific angular momentum decreases due to emission of gravitational waves. Hence, a disk can be formed only in the case (i) an efficient mechanism for angular momentum transport which works within ~ 1 ms after the onset of the merger (before collapsing to a black hole) is present and (ii) the transport mechanism works efficiently enough for overcoming the dissipation by gravitational radiation in the outer region. For $Q_M \sim 1$, angular momentum transport due to a torque by the nonaxisymmetric central object does not work efficiently, resulting in the small disk mass.

We note that in the prompt formation of a black hole, the time for the angular momentum transport is much shorter than in the formation of a hypermassive neutron star. This is the main reason that the disk mass is much smaller than that in Sec. IV B 3 for nearly equal-mass binaries.

For $Q_M \lesssim 0.9$, the disk mass increases with decreasing the value of Q_M because the less massive neutron star is tidally elongated at the merger, and hence, efficiency of the angular momentum transport is enhanced. However, the disk mass does not exceed $0.01M_\odot$ even for $Q_M = 0.75$ for the APR EOS. The likely reason is that the stellar radius is small irrespective of the mass of each star in this EOS. Due to this property, the merged object

is compact at the onset of merger enough to promptly produce a black hole without transporting angular momentum efficiently.

The disk mass is much larger in the SLy EOS for a given value of Q_M than in the APR EOS. The reasons are (i) the mass ($M \approx 2.76M_\odot$) is smaller than for the APR EOS case ($M \approx 2.96M_\odot$) and (ii) with the SLy EOS, the stellar radius of relatively small mass $M \lesssim 1.3M_\odot$ is larger (cf. Fig. 2). With the smaller mass, the gravitational radiation reaction time scale is longer. Consequently, the less massive star in the binary is tidally elongated by a larger degree, slightly postponing the collapse of the merged object to a black hole and enhancing efficiency of the angular momentum transport.

It is interesting to note that the disk mass decreases during the growth of a black hole in the following mechanism: In the merger of unequal-mass binary, the less massive neutron star is always tidally elongated. The inner part first collides the companion, but slips through the companion's surface to form a small spiral arm around a black hole which is subsequently born. Outer part of larger angular momentum also forms a large spiral arm. The phase difference between these two spiral arms is about 180° at their formation (cf. Figs. 6–8). However, since the smaller spiral arm rotates faster than the larger one, the two spiral arms collide each other to generate shocks in one rotational period, which convert a large fraction of the kinetic energy to the thermal energy. As a result, an amount of matter is swallowed into the black hole quickly. The collision of the spiral arms also leads to geometrical thickening of the disk [cf. Fig. 9(e) and (f)] as well as to the heat-up.

For $M \approx 2.96M_\odot$ in the APR EOS and $M \approx 2.76M_\odot$ in the SLy EOS, the numerical results of the disk mass M_d as a function of Q_M for $0.75 \lesssim Q_M \leq 1$ is approximately fitted by

$$M_d = M_{d0} + M_{d1}(1 - Q_M)^p, \quad (29)$$

where $M_{d0} = 0.0004M_\odot$, $M_{d1} \approx 1.44M_\odot$, and $p = 4$ for $M \approx 2.96M_\odot$ in the APR EOS with (633, 633, 317) grid size, and $M_{d0} = 0.003M_\odot$, $M_{d1} \approx 3.33M_\odot$, and $p = 3$ for $M \approx 2.76M_\odot$ in the SLy EOS with (377, 377, 189) grid size. Since M_{d0} is small, M_d is approximately proportional to $(1 - Q_M)^p$ for $Q_M \lesssim 0.8$, and hence, the value of M_{d1} essentially determines the relation. As mentioned previously, the value of M_d varies by $\sim 30\%$ depending on the grid size by which the radiation reaction time scale and resulting transport time of the angular momentum spuriously change.

As indicated by this fitting formulae (29), the disk mass steeply increases with decreasing the value of Q_M (cf. Fig. 13), although for $Q_M \gtrsim 0.9$, the disk mass is much smaller than $0.01M_\odot$. For $Q_M \lesssim 0.7$, the increase rate of M_d with decreasing value of Q_M is not as steep as Eq. (29), but it is still positive.

We note that the disk mass obtained here for the prompt black hole formation case gives an approximate upper limit for both the APR and SLy EOSs, since the

ADM mass adopted is close to M_{thr} . For more massive case, the system at the merger becomes more compact and has a shorter dynamical time scale. Therefore, outward transport of angular momentum works for a shorter time scale, resulting in smaller disk mass.

Figure 10(b) shows the angular velocity of the disk for model APR135165 and illustrates that the disk approximately has the Kepler angular velocity for the radius larger than ~ 10 km which is approximately the radius of the ISCO around the black hole. The angular velocity of the inner part with $R \lesssim 10$ km is not as large as the Kepler one, indicating that matter in such region gradually falls into the central black hole. This is also seen from the velocity fields in Fig. 9(d)–(f). In reality, the matter in the accretion disk of the Kepler angular velocity will subsequently evolve in a dissipation time scale, which is determined either by viscosity or by magnetic fields.

For $Q_M \gtrsim 0.9$, not only the disk mass is small but also the disk is geometrically thin. These properties are completely unfavored for producing high-Lorentz factor jets of GRBs [6]. Therefore, prompt formation of a black hole in the merger of binary neutron stars of the mass ratio $Q_M \gtrsim 0.9$ is unlikely to be a scenario for producing a central engine of SGRBs. On the other hand, for a sufficiently small value of Q_M ($Q_M \lesssim 0.75$ for the APR EOS and $Q_M \lesssim 0.85$ for the SLy EOS), the disk mass will be larger than $\sim 0.01M_\odot$. In addition, the disk is geometrically thick as indicated in Fig. 9(f) for model APR1317; i.e., a torus is formed. Furthermore, the thermal energy, which is generated in the shock heating between spiral arms in the disk and is evaluated from $\varepsilon - \varepsilon_{\text{cold}}$ [21], is high enough (typically $\sim 1\text{--}2 \times 10^{11}$ K) for generating a large amount of thermal neutrinos [10, 60]. Viscous heating will also play a role for subsequently keeping such high temperature. Implication of such hot torus with mass $\gtrsim 0.01M_\odot$ will be given in Sec. IV D.

2. Properties of black hole

The area of the apparent horizon A_{AH} is determined in the black hole formation cases. From the area A_{AH} , the irreducible mass may be approximately defined by

$$M_{\text{irr}} \approx \sqrt{\frac{A_{\text{AH}}}{16\pi}}, \quad (30)$$

which varies from $0.9M_0$ to $0.97M_0$ for all the models in the APR EOS as shown in Fig. 12(b). Since most of the fluid elements are swallowed into the black hole and, also, the energy carried out by gravitational radiation is $\approx 0.01M_0$ (see Sec. V), the mass of the formed black hole should be approximately $\sim 0.99M_0$. Assuming that the area of the apparent horizon is equal to that of the event horizon, the non-dimensional spin parameter of the black hole is defined by $q \equiv J_{\text{BH}}/M_{\text{BH}}^2$ where J_{BH} and M_{BH} are the angular momentum and the ADM mass of

the black hole. Then the irreducible mass is defined in terms of q and M_{BH} by

$$M_{\text{irr}} = \sqrt{\frac{1 + (1 - q^2)^{1/2}}{2}} M_{\text{BH}}. \quad (31)$$

Equation (31) implies that for $M_{\text{irr}}/M_0 = 0.9\text{--}0.97$, $q = 0.8\text{--}0.4$. This indicates that the small error in the estimation for M_{irr} leads to a large error in q estimated from the area of the apparent horizon. To reduce the error, the simulation should be performed with a better grid resolution. For this purpose, an adaptive mesh refinement technique will be helpful [61], but the simulation with such technique is beyond the scope of this paper.

The value of q is also approximately determined from the following manner. As shown in Sec. V, the angular momentum is dissipated by $\sim 15\%$ by gravitational radiation, while the ADM mass decreases by $\sim 1\%$ throughout the simulation. As listed in Table II, the initial value of q is ≈ 0.9 . Therefore, the value of q in the final stage should be ≈ 0.75 for which $M_{\text{irr}} \approx 0.91 M_{\text{BH}}$. Assuming that this is the correct value, the error in the irreducible mass of the black hole determined from the area of the apparent horizon is within $\sim 5\%$.

Given the spin parameter $q = 0.7\text{--}0.8$ and the ADM mass $M_{\text{BH}} \approx 2.8 M_{\odot}$, the frequency of the fundamental quasinormal mode is about $6.5\text{--}7(2.8 M_{\odot}/M_{\text{BH}})$ kHz [62]. We will show the ring-down gravitational waves with this frequency in Sec. V.

D. Implication to SGRBs

As shown in sections IV B and IV C (also illustrated in previous papers [21, 57]), merger of binary neutron stars can produce a system composed of a Kerr black hole and a hot torus of mass $\gtrsim 0.01 M_{\odot}$ if certain condition is satisfied. To summarize, there are following two scenarios to achieve the formation of a massive disk with $M_d \geq 0.01 M_{\odot}$: (i) In the first scenario, a hypermassive neutron star is required to be formed first. Then, by some mechanisms, the angular momentum is transported from the inner region to the outer envelop which subsequently forms a hot disk (torus), while the hypermassive neutron star eventually collapses to a black hole either by angular momentum dissipation due to gravitational radiation or by angular momentum transport probably due to magnetic effects [23]. In this scenario, the estimated torus mass will be $\sim 0.01\text{--}0.03 M_{\odot}$ in the absence of strong magnetic effects, while in its presence, the mass can be $\gtrsim 0.05 M_{\odot}$ [56, 57]. (ii) In the second scenario, a black hole is promptly formed after the onset of merger in an unequal-mass binary of sufficiently small mass ratio Q_M . Then, a torus is formed from the less massive neutron star which is tidally elongated at the merger and subsequently constitutes a hot and geometrically thick torus. In this case, the torus mass depends strongly on the value of Q_M and nuclear EOSs.

In [57], a scenario through formation of a hypermassive neutron star with strong magnetic fields is described. In this case, a large accretion rate from the torus to the black hole with $\dot{M} \gtrsim 5 M_{\odot}/\text{s}$ is expected. In the rest of this section, we focus mainly on other scenarios with no strong magnetic fields; in particular, we focus on scenario (ii).

In the following, we assume that the disk mass is $M_d \sim 0.01\text{--}0.1 M_{\odot}$ and mass accretion rate is $\dot{M} \sim 0.1\text{--}1 M_{\odot}/\text{s}$. These are plausible values for a central engine of SGRBs since the life time of torus becomes $t_{\text{dur}} \sim 10\text{--}1,000$ ms with such choice. The transport time of the angular momentum used here for \dot{M} is assumed to be determined by an appropriate value of the viscosity or moderately strong magnetic fields as in the α -viscosity model [63].

The gravitational binding energy W of disk with mass $\sim 0.01\text{--}0.1 M_{\odot}$ in the black hole spacetime is

$$W \sim \frac{M_{\text{BH}} M_d}{r_d} \approx 2 \times 10^{51} \text{ ergs} \left(\frac{10 M_{\text{BH}}}{r_d} \right) \left(\frac{M_d}{0.01 M_{\odot}} \right), \quad (32)$$

where r_d denotes an averaged disk radius. Due to viscous dissipation in the accretion disk, the kinetic energy is converted to the thermal energy. Equation (32) indicates that the total thermal energy produced during the accretion will be $\sim 10^{51}\text{--}10^{52}$ ergs, which is $10^2\text{--}10^5$ times larger than the total radiated energy in SGRBs (for the value after correction of a beaming factor) [8]. Therefore, a relativistic fireball of sufficient energy may be formed if there is a mechanism by which a fraction of the thermal energy is converted to the fireball. In the past several years, scenarios for producing such fireball have been indeed proposed [10, 60, 64, 65, 66, 67, 68, 69]. We describe a scenario following a semianalytic calculation [67]. More detailed numerical simulations have been performed recently [68, 69]. According to these numerical works, the neutrino luminosity can be by a factor of ~ 10 larger than that in [67] if the mass of disk is sufficiently large $\gtrsim 0.05 M_{\odot}$. Thus, the luminosity described below may be considered as a conservative value.

Because of its high temperature (typically $\sim 10^{11}$ K) and density ($\sim 10^{11}$ g/cm³; cf. Figs 7, 8, and 9(d)–(f)), the torus radiates strongly in thermal neutrinos. The opacity inside the torus (considering only neutrino absorption and scattering interactions with nucleons) is $\kappa \sim 7 \times 10^{-17} (T/10^{11} \text{ K})^2 \text{ cm}^2 \text{ g}^{-1}$ [64, 67] where T is the temperature. To estimate the optical depth, we define the surface density of torus by

$$\Sigma(x, y) = \int_{z \geq 0} \rho u^t \sqrt{-g} dz, \quad (33)$$

where the integral is carried out along lines of $x = y = \text{constant}$. For $M_d \gtrsim 0.01 M_{\odot}$ (e.g., for models APR1317, APR127175, APR1218, SLy1315, SLy125155, SLy1216), $\Sigma \gtrsim 10^{17}$ g/cm², so that the optical depth

of the neutrinos $\sim \kappa\Sigma$ is $\gtrsim 1$ for $r \lesssim 20 \text{ km} \approx 5M_{\text{BH}}$. This optical depth is in approximate agreement with the model presented in [67]. (Note that in a high viscosity case, the significant increase of the thermal pressure by the viscous dissipation may enforce the torus to expand and to decrease the optical depth below unity [68]).

In the optically thick case, approximate neutrino luminosity may be estimated in the diffusion limit [70] as $L_\nu \sim \pi r_d^2 F$ where F is the neutrino flux from the torus surface, approximately estimated by

$$F \sim \frac{7N_\nu}{3} \frac{\sigma T^4}{\kappa\Sigma}. \quad (34)$$

Here, σ denotes the Stefan-Boltzmann constant and N_ν is the number of neutrino species, taken as 3. Then, the neutrino luminosity is expressed as

$$L_\nu \sim 2 \times 10^{52} \text{ ergs/s} \left(\frac{r_d}{10 \text{ km}} \right)^2 \times \left(\frac{T}{10^{11} \text{ K}} \right)^2 \left(\frac{\Sigma}{10^{17} \text{ g/cm}^2} \right)^{-1}, \quad (35)$$

which is only slightly smaller than the neutrino Eddington luminosity [67]. Hence, our numerical results suggest formation of a hot, hyperaccreting torus which is optically thick to neutrinos. A model for the neutrino emission in a similar flow environment with comparable L_ν is provided in [67] as a neutrino-dominated accretion flow (NDAF).

According to the model of [67], the luminosity due to neutrino-antineutrino ($\nu\bar{\nu}$) annihilation is [67]

$$L_{\nu\bar{\nu}} \sim 10^{49} - 10^{50} \text{ ergs/s}, \quad (36)$$

for $\dot{M} \sim 0.1 - 1M_\odot/\text{s}$. (The work in [64, 67] also indicates that for $\dot{M} < 0.1M_\odot/\text{s}$, the luminosity steeply decreases far below $L_{\nu\bar{\nu}} = 10^{49} \text{ ergs/s}$.) In our model, the black hole is rapidly rotating with $q \sim 0.75$, and hence, the luminosity may be enhanced by a factor of several due to a GR effect [64]. Also, in a more careful estimation for the neutrino annihilation and for the neutrino opacity than those in [67], the value of $L_{\nu\bar{\nu}}$ could be increased by a factor of ~ 10 [68, 71].

Because of the thick geometry of the torus, pair $\nu\bar{\nu}$ annihilation will be most efficient near the z -axis and just above the surface of the inner region of the torus [68, 71] for which the density is much smaller than that of the torus. Consequently, the baryon-loading problem [6] will be escaped, and hence, a strongly relativistic fireball is likely to be produced.

Aloy et al. [72] simulate the propagation of jets powered by energy input along the rotation axis (as would be supplied by the $\nu\bar{\nu}$ annihilation). They find that if the half-opening angle of the energy injection region is moderately small ($\lesssim 45^\circ$) and the baryon density around the black hole is sufficiently low, jets with the Lorentz factors in the hundreds can be produced given an energy input $L_{\nu\bar{\nu}} \approx 10^{49} - 10^{50} \text{ ergs/s}$ lasting $\sim 100 \text{ ms}$. In such case,

the conversion rate from the pair annihilation luminosity to the jet energy is a few $\times 10\%$ in their results. They also indicate that the duration of SGRBs may be ~ 10 times longer than the duration of the energy input because of the differing propagation speeds of the jet head and tail; namely, duration of the energy supply with $\sim 10 \text{ ms}$ may be sufficient for explaining a SGRB with duration $\sim 100 \text{ ms}$.

Our numerical results, along with the accretion flow (NDAF) [67] and jet propagation models of [72], thus suggest that the system composed of a black hole and hot torus with $M_d \gtrsim 0.01M_\odot$ and accretion rate $\dot{M} \sim 0.1 - 1M_\odot/\text{s}$ is a possible candidate for the central engine of SGRBs. Since the lifetime of the torus is $\gtrsim 10 - 100 \text{ ms}$ in our model, the total energy of the $\nu\bar{\nu}$ annihilation is $E_{\nu\bar{\nu}} \sim 10^{48} \text{ ergs}(M_d/0.01M_\odot)$. Typical total energy of SGRBs are several $\times 10^{48} \text{ ergs}$ [8], and hence, a system of the disk mass $\sim \text{several} \times 0.01M_\odot$ is likely to be appropriate for powering SGRBs as long as the emission is beamed. Probably, beaming is encouraged by the thick geometrical structure of the torus [72].

The above discussion suggests that if the mass ratio is sufficiently small, prompt formation of a black hole may be a possible scenario for producing the central engine of SGRBs. In particular, for a small value of $Q_M \lesssim 0.8$ with the SLy EOS, a large SGRB energy is expected. Unfortunately, binary neutron stars of small mass ratio with $Q_M < 0.9$ have not been found so far [49]. Hence, it is not clear at present whether the formation rate of such unequal-mass binary is large enough for explaining the event rate of SGRBs. This is a weak point in this scenario.

Through formation of a hypermassive neutron star with moderately strong magnetic fields, a system composed of a black hole and a disk of mass $\sim 0.01 - 0.03M_\odot$ may be formed as discussed in Sec. IV B. The estimation described in this section is also applied for such system, and indicates that a central engine of SGRBs of relatively low total energy $\sim \text{several} \times 10^{47} - 10^{48} \text{ ergs}$ could be formed. If the time scale of the angular momentum transport by the magnetic effects (or viscosity) is longer than emission time scale of gravitational waves, a black hole is formed (i.e., a SGRB should be generated) after a longterm emission of quasiperiodic gravitational waves from the hypermassive neutron star. As we will discuss in Sec. V, such gravitational waves may be detected by advanced laser-interferometric detectors. If quasiperiodic gravitational waves and subsequent SGRB are detected coincidentally in the same direction with a small time lag, thus, this scenario may be confirmed.

The results for the disk mass in this paper suggest that a merger between a black hole and a neutron star could form a system composing a black hole and surrounding massive disk by tidal disruption [73]. Indeed, if the mass of the black hole is small enough [$M_{\text{BH}} \lesssim 4M_\odot(R_0/10 \text{ km})^{3/2}$ for $q = 0$ and $M_{\text{BH}} \lesssim 20M_\odot(R_0/10 \text{ km})^{3/2}$ for $q = 0.9$ where q and R_0 are a spin parameter of the black hole and a neutron star

radius [74]], the neutron star will be tidally disrupted before reaching the ISCO. If the event rate (though it is not clear at present because black hole-neutron star binary has not been observed so far) is large enough, such a merger could be a promising source for producing a central engine of SGRBs. However, a detailed simulation in full general relativity is necessary to confirm this scenario since the disk mass depends crucially on the location of the ISCO.

V. GRAVITATIONAL WAVEFORMS

A. Gravitational waves from hypermassive neutron stars

1. Waveform and luminosity

In Fig. 14, we present gravitational waveforms in the formation of hypermassive neutron stars (models APR1313 and APR1414) as a function of a retarded time. Throughout this paper, the retarded time t_{ret} is defined by $t - r_{\text{obs}}$ where r_{obs} is the coordinate radius of the wave extraction. In the early phase ($t_{\text{ret}} \lesssim 2$ ms), gravitational waves associated with the inspiral motion are emitted, while for $t_{\text{ret}} \gtrsim 2$ ms, those by the rotating and oscillating hypermassive neutron star are emitted. In the following, we focus only on the waveforms for $t_{\text{ret}} \gtrsim 2$ ms.

For model APR1313, a hypermassive neutron star of ellipsoidal shape is formed after the merger sets in. As a result, quasiperiodic gravitational waves with an approximately constant frequency ≈ 3.2 kHz are emitted. Also, the amplitude remains approximately constant for $t \gtrsim 5$ ms. These properties are essentially the same as those found in [21] for models SLy1313 and SLy125135.

For model APR1414, on the other hand, the amplitude decreases with time in particular for $t > 6$ ms. This reflects the fact that the ellipticity of the formed hypermassive neutron star steeply decreases for $t \gtrsim 6$ ms. This indicates that only less massive binaries can produce a longterm emitter of quasiperiodic gravitational waves. For model APR1414, the frequency is not constant either, but modulates with time as in model SLy135135 [21]. The reason is that the formed hypermassive neutron star quasiradially oscillates with a large amplitude and the characteristic frequency varies with the change of the characteristic radius. Due to this, the shape of the Fourier spectra for models APR1313 and APR1414 are different even qualitatively (cf. Fig. 17). Namely, for $M \lesssim M_{\text{thr}}$, a slight difference in the total ADM mass results in a significant difference in gravitational waveforms.

In Fig. 15, the emission rates of the energy and the angular momentum by gravitational radiation are shown for models APR1313 (solid curves) and APR1414 (dashed curves). In the inspiral phase for $t_{\text{ret}} \lesssim 2$ ms, the emission rates increase with time (besides initial unphysical bump associated with the conformal flat initial condition

in which gravitational waves are neglected), since the amplitude and the frequency of the chirp signal increase. Then the peak is reached at $t_{\text{ret}} \sim 2$ ms. The height of the peak is larger for model APR1414 since the compactness of each star is larger. After the peak is reached, the emission rates once quickly decrease since the merged object becomes a spheroidal transient object. However, because of its large angular momentum and stiff EOS, the formed hypermassive neutron star soon changes to a highly ellipsoidal object which emits gravitational waves of a large amplitude. The luminosity from the ellipsoidal neutron star is as high as the first peak at $t_{\text{ret}} \sim 2.5$ ms for model APR1414 and at $t_{\text{ret}} \sim 3.5$ ms for model APR1313.

After the second peak, the emission rates of the energy and the angular momentum via gravitational waves gradually decrease with time, since the degree of the non-axial symmetry decreases. However, for model APR1313, the decrease rates are small and the emission rates at $t_{\text{ret}} \sim 10$ ms remain to be as high as that in the late inspiral phase as $dE/dt \sim 6 \times 10^{54}$ erg/s and $dJ/dt \sim 6 \times 10^{50}$ g cm²/s² reflecting the high ellipticity of the hypermassive neutron star. The angular momentum at $t \sim 10$ ms is $J \sim 0.7J_0 \sim 4 \times 10^{49}$ g cm²/s. Assuming that the emission rate of the angular momentum remains $\sim 5 \times 10^{50}$ g cm²/s and that emission stops when about half of J is dissipated, the emission time scale is approximately evaluated as $J/(2dJ/dt) \sim 40$ ms. If the nonaxisymmetric structure is maintained and dJ/dt does not vary much, thus, the hypermassive neutron star will collapse to a black hole within ~ 50 ms even in the absence of other dissipation processes (cf. the discussion in the last paragraph of IV B 1).

For model APR1414, on the other hand, the emission rates decrease quickly since the hypermassive neutron star relaxes to an approximately axisymmetric spheroid for $t \gtrsim 6$ ms. For this model, the dissipation time scale of the angular momentum is much longer than 50 ms at $t = 10$ ms. Therefore, other dissipation processes such as magnetically induced angular momentum transport will trigger the collapse to a black hole.

By the time integral of dE/dt and dJ/dt , the total energy and angular momentum radiated are computed and found to be about $0.03M_0$ and $0.30J_0$ for model APR1313 and $0.03M_0$ and $0.26J_0$ for model APR1414, respectively. This indicates that the angular momentum is significantly dissipated, illustrating that the angular momentum dissipation plays an important role in the evolution of the system. To confirm that the radiation reaction is followed in the simulation, we display $J(t)$ and $J_0 - \Delta(t)$ as a function of time for models APR1313 and APR1414 in Fig. 16. This shows that the angular momentum computed from Eq. (20) agrees approximately with $J_0 - \Delta J$ (within $\sim 2\%$ error), proving that radiation reaction is computed with a good accuracy.

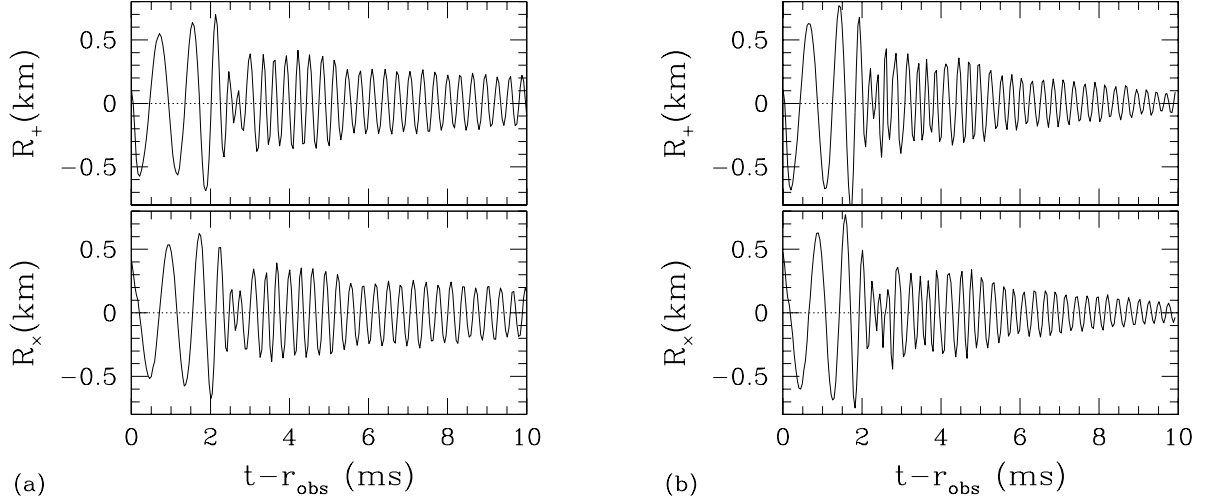


FIG. 14: Gravitational waveforms, R_+ and R_x , (a) for model APR1313 at $r_{\text{obs}} = 36M_0$ and (b) for model APR1414 at $r_{\text{obs}} = 32M_0$.

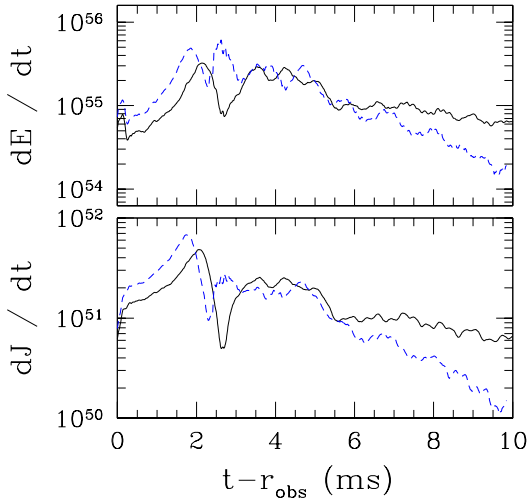


FIG. 15: Energy and angular momentum emission rates, dE/dt and dJ/dt , of gravitational waves for models APR1313 (solid curves) and APR1414 (dashed curves). The units are erg/s and g cm²/s², respectively.

2. Fourier spectrum

In the real data analysis of gravitational waves, a matched filtering technique [3] is employed. In this method, the signal of the identical frequency can be accumulated using appropriate templates. As a result, the effective amplitude increases by a factor of $N^{1/2}$ where N denotes an approximate number of the cycle of gravitational waves for a given frequency.

To determine the characteristic frequency of gravitational waves, we carry out a Fourier analysis. In Fig. 17, the power spectrum dE/df is presented for models APR1313 and APR1414. Since the simulations were

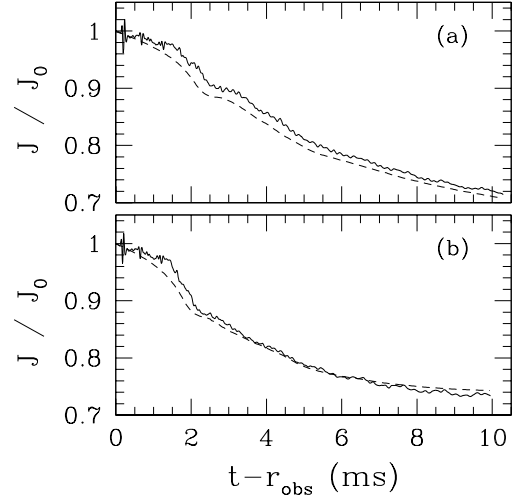


FIG. 16: The solid curve denote evolution of angular momentum for models (a) APR1313 and (b) APR1414. The dashed curves denote $J_0 - \Delta J$ where J_0 denotes the angular momentum at $t = 0$.

started with the initial condition of the orbital period ~ 2 ms (i.e., frequency of gravitational waves is ~ 1 kHz), the spectrum of inspiraling binary neutron stars for $f < 1$ kHz cannot be correctly computed. Thus, only the spectrum for $f \gtrsim 1$ kHz should be paid attention. As a plausible spectrum for $f \lesssim 1$ kHz, we plot the Fourier power spectrum of two point particles in circular orbits in the second post Newtonian approximation (the dotted curve) [75] (the third post Newtonian terms does not significantly modify the spectrum since their magnitude is ~ 0.01 of the leading-order term).

Figure 17 shows that a sharp characteristic peak is present at $f \approx 3.2$ and 3.8 kHz for models APR1313 and APR1414, respectively. This is associated with quasiperi-

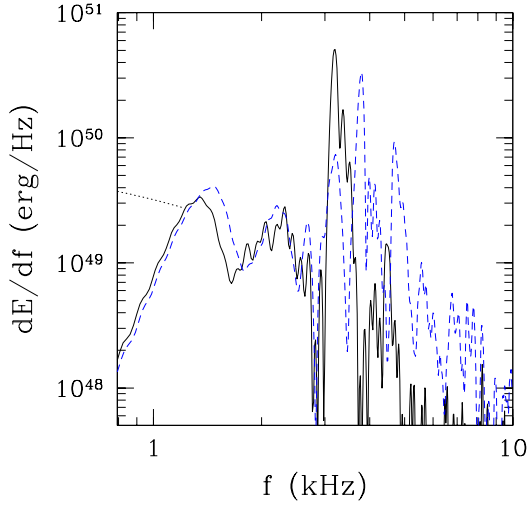


FIG. 17: Fourier power spectrum of gravitational waves dE/df for models APR1313 (solid curve) and APR1414 (dashed curve). Since the simulations are started when the characteristic frequency of gravitational waves is ~ 1 kHz, the spectrum for $f < 1$ kHz cannot be presented. The dotted curve in the panel denotes the analytical result of dE/df in the second post Newtonian and point-particle approximation by which the real spectrum for $f \lesssim 1$ kHz is approximated.

odic gravitational waves emitted by the formed hypermassive neutron stars. Two side-band peaks are present at $f \approx 3.2$ and 4.7 kHz for model APR1414. Thus, the spectral shape is qualitatively different from that for model APR1313. The reason is that the amplitude of the quasiradial oscillation of the hypermassive neutron star is outstanding and the characteristic radius varies for a wide range for model APR1414, inducing the modulation of the wave frequency.

An effective amplitude of gravitational waves observed from the most optimistic direction (which is parallel to the axis of the angular momentum) is proportional to $\sqrt{dE/df}$ in the manner

$$h_{\text{eff}} \equiv \sqrt{|\bar{R}_+|^2 + |\bar{R}_\times|^2} f$$

$$= 1.8 \times 10^{-21} \left(\frac{dE/df}{10^{51} \text{ erg/Hz}} \right)^{1/2} \left(\frac{100 \text{ Mpc}}{r} \right) (37)$$

where r denotes the distance from the source, and $\bar{R}_{+,\times}$ are the Fourier spectrum of $R_{+,\times}$. In Fig. 18, we show h_{eff} as a function of f for a hypothetical distance of 50 Mpc. This shows that the effective amplitude of the peak is ~ 3 times larger than that at ~ 1.3 – 1.5 kHz which corresponds to the frequency of the last inspiral motion.

For model APR1313, furthermore, the amplitude of the peak in reality should be larger than that presented here, since we stopped simulations at $t \sim 10$ ms to save the computational time, and hence, the integration time (~ 10 ms) is much shorter than the realistic value. Extrapolating the decrease rate of the angular momentum, the hypermassive neutron star will dissipate sufficient an-

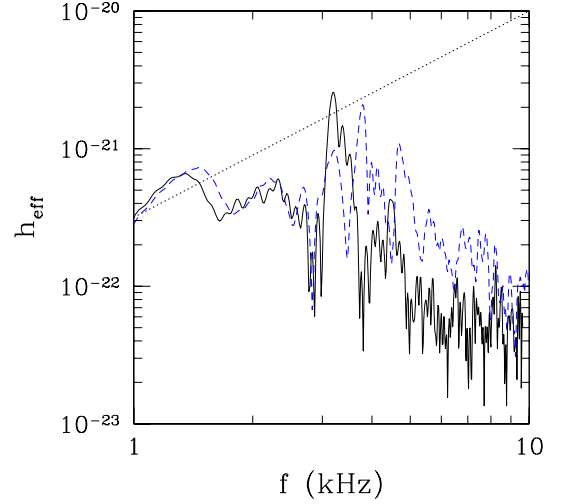


FIG. 18: Non-dimensional effective amplitude of gravitational waves from hypermassive neutron stars for models APR1313 (solid curve) and APR1414 (dashed curve). The assumed distance is 50 Mpc. The dotted line denotes the planned noise level of the advanced LIGO.

gular momentum by gravitational radiation until a black hole or a spheroidal star is formed. As indicated in Sec. V A 1, the duration of the angular momentum dissipation would be ~ 50 ms. Thus, we may expect that the emission will continue for such time scale and the effective amplitude of the peak would be in reality amplified by a factor of $\sim 5^{1/2} \approx 2$ to be $\sim 6 \times 10^{-21}$ at a distance of 50 Mpc. Although the sensitivity of laser-interferometric gravitational wave detectors for $f > 1$ kHz is limited by the shot noise of the laser, this value is by a factor of 3–4 larger than the planned noise level of the advanced LIGO $\approx 10^{-21.5} (f/1 \text{ kHz})^{3/2}$ [3]. It will be interesting to search for such quasiperiodic signal of high frequency if the chirp signal of gravitational waves from inspiraling binary neutron stars of distance $r \lesssim 50$ Mpc are detected in the near future. As discussed in [24], the detection of such quasiperiodic signal leads to constraining nuclear EOSs for neutron star matter. Furthermore, as mentioned in Sec. IVD, the detection may also lead to confirming a scenario for producing the central engine of SGRBs.

On the other hand, for model APR1414, the quasiperiodic gravitational waves damp at $t \sim 6$ ms, and hence, the expected amplitude is $h_{\text{eff}} \sim 2 \times 10^{-21}$ at a distance of 50 Mpc with $f \sim 4$ kHz. If the required signal to noise ratio of gravitational waves for confirming the detection is ~ 5 in the advanced LIGO, such signal will be detected only for an event within the distance ~ 10 Mpc. Since the predicted event rate of the merger for such distance is $\lesssim 0.01$ per years [2], frequent detection is not expected. However, the fortunate detection may lead to confirming a scenario for producing the central engine of SGRBs.

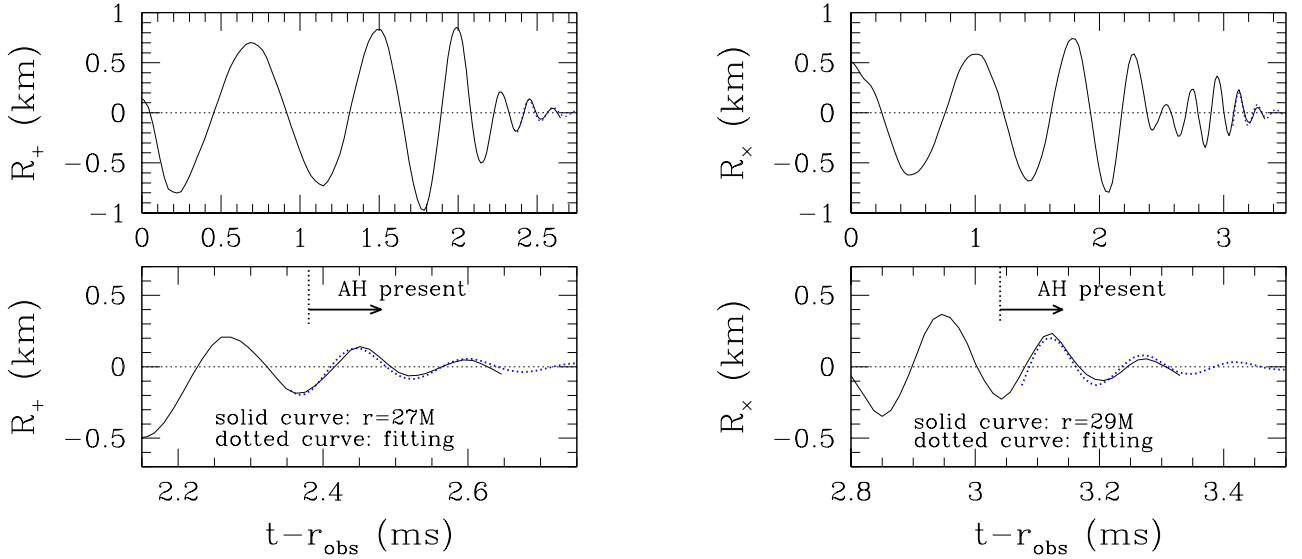


FIG. 19: The same as Fig. 14, but for models APR135165 (left) at $r_{\text{obs}} = 27M_0$ and model SLy125155 at $r_{\text{obs}} = 29M_0$ (right). The lower panel is the enlargement of the upper panel for ring-down gravitational waves associated with a quasinormal mode of the formed black hole. The formation time of the apparent horizon t_{AH} is 2.38 ms for model APR135165 and 3.04 ms for model SLy125155, and hence, the quasinormal mode is excited for $t - r_{\text{obs}} \gtrsim t_{\text{AH}}$. The thick dotted (blue) curves denote the fitting formulae described by Eq. (38).

B. Gravitational waves in the black hole formation

In the prompt formation of a black hole, ring-down gravitational waveforms associated with a quasinormal mode is emitted. Figure 19 shows R_+ for model APR135165 and R_x for model SLy125155 as a function of retarded time. In the early time ($t_{\text{ret}} \lesssim 2$ ms for model APR135165 and $t_{\text{ret}} \lesssim 2.3$ ms for model SLy125155), gravitational waveforms are determined by the inspiraling motion. After this, a merger waveform, which is emitted due to hydrodynamic interaction between two stars, is seen for a short time scale ~ 0.5 ms. The merger waveform is emitted for a longer time for model SLy125155 simply because the time from the onset of the merger to formation of a black hole is longer. Finally, a black hole is formed and the waveforms are determined by the fundamental quasinormal mode. The formation time of the apparent horizon t_{AH} is 2.38 ms for model APR135165 and 3.04 ms for model SLy125155. Assuming that the formation time of the event horizon is approximately the same, ring-down waveforms associated with the quasinormal mode should be induced only for $t_{\text{ret}} \gtrsim t_{\text{AH}}$. In our numerical results, this condition indeed holds, and therefore, we have confirmed that the quasinormal mode is extracted [76].

For models APR1416, APR135165, APR1317, and SLy125155, the initial values of the non-dimensional angular momentum parameter q_0 is ≈ 0.9 . The energy and the angular momentum are dissipated by gravitational waves by $\sim 0.01M_0$ and $0.15J_0$ until formation of the black holes (cf. Fig. 20). Taking into account the fact that a tiny fraction of mass and angular momentum is

distributed to the surrounding disk, the spin parameter of the formed black hole should be ~ 0.75 . The dotted curve in Fig. 19 denotes a model of ring-down gravitational waveforms

$$Ae^{-(t-t_{\text{AH}})/t_d} \cos(2\pi f_{\text{qnm}}t + \delta), \quad (38)$$

where A denotes the maximum amplitude and δ a phase constant. f_{qnm} and t_d are the frequency and damping rate of ring-down gravitational waves of $l = m = 2$ mode, which are approximately given by [62]

$$f_{\text{qnm}} \approx 10.8 \left(\frac{M}{3M_\odot} \right)^{-1} [1 - 0.63(1 - q)^{0.3}] \text{ kHz}, \quad (39)$$

$$t_d \approx \frac{2(1 - q)^{-0.45}}{\pi f_{\text{qnm}}}. \quad (40)$$

For $M = 2.9M_\odot$ and $q = 0.75$, $f_{\text{qnm}} = 6.5$ kHz and $t_d = 0.183$ ms which are used for the fitting to the waveform of model APR135165. For model SLy125155, we plot the curve with $M = 2.7M_\odot$ and $q = 0.7$, and hence, $f_{\text{qnm}} = 6.7$ kHz and $t_d = 0.163$ ms. This illustrates that with $M = 2.7\text{--}2.9M_\odot$, the frequency will be in a small range between 6.5 and 7 kHz.

In Fig. 19, the fitting formulae are plotted together. It shows that the computed waveforms agree approximately with the fitting curves. This implies that gravitational waves numerically extracted carry the information of the formed black hole correctly. The maximum value of $R_{+,x}$ in the ring-down phase is ~ 0.15 km for model APR135165 and ~ 0.25 km for model SLy125155, implying that the maximum amplitude is $\sim 1\text{--}2 \times 10^{-22}$ at a distance of 50 Mpc [cf. Eq. (17)]. These values depend weakly on the mass ratio. The amplitude in model

SLy125155 is slightly larger than that in the APR EOS. This is probably because the accretion rate of the matter which can excite the quasinormal mode is larger in the SLy EOS.

Since the frequency is too high and the amplitude is too small, it will be difficult to detect ring-down gravitational waves even by advanced laser-interferometric gravitational wave detector. Only in the case that a merger happens in our local group, it may be detected. However, the expected event rate is less than 0.001 /yrs [2].

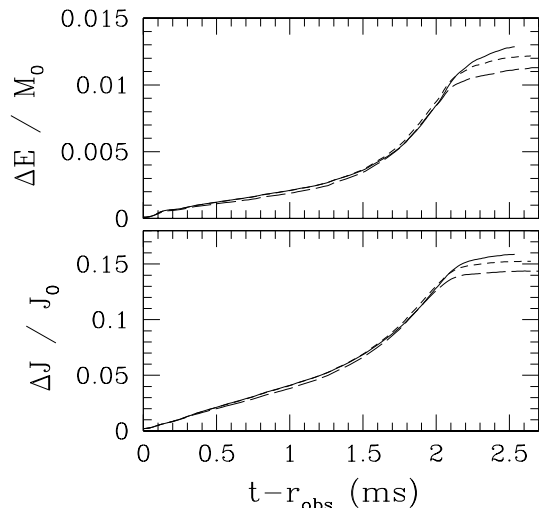


FIG. 20: Evolution of the total radiated energy ΔE and angular momentum ΔJ for models APR1416 (solid curves), APR135165 (dashed curves), and APR1317 (long dashed curves)

Figure 20 shows the evolution of radiated energy and angular momentum by gravitational waves for models APR1416, APR135165, and APR1317. It is found that $\sim 1\%$ of the total mass energy and $\sim 15\%$ of the angular momentum are dissipated by gravitational waves. These gravitational waves are mostly emitted in the last one inspiral orbits and the contribution from the ring-down phase is negligible. (For model SLy125155, the results are quantitatively the same as those of APR models.) The significance of the dissipation of the angular momentum in the last orbit should be emphasized since it affects the mass of disks surrounding the formed black hole. Another important property found from Fig. 20 is that for smaller mass ratios, the radiated energy and angular momentum are smaller. This results from the fact that with the smaller mass ratios, the tidal elongation sets in at a larger orbital separation, and hence, the inspiral waveform shuts off earlier [17, 79, 80].

VI. SUMMARY

As an extension of our previous work [21], we performed fully general relativistic simulations for the merger of binary neutron stars adopting stiff nuclear

EOSs. We focus particularly on the formation of a black hole and surrounding disk in this paper. The following is the summary of the new results described in this paper. The summary about the outcome after the merger is also described in Fig. 21.

1. Threshold mass for black hole formation

In the APR EOS which is mainly adopted in this paper, the threshold mass for prompt formation of a black hole is $M_{\text{thr}} \approx 2.8\text{--}2.9M_{\odot}$ which is about 30–35 % larger than the maximum mass for spherical neutron stars with identical EOS, M_{sph} . Collecting the results obtained in [21], we conclude that the following relation holds for stiff nuclear EOSs such as FPS, SLy, and APR EOSs: $M_{\text{thr}} = 1.3\text{--}1.35M_{\text{sph}}$.

2. Formation of hypermassive neutron star ($M < M_{\text{thr}}$)

If $M < M_{\text{thr}}$, a hypermassive neutron star is formed as an outcome of the merger. If the mass is not close to M_{thr} , the outcome has an ellipsoidal shape, and hence, is a strong emitter of quasiperiodic gravitational waves. Because of angular momentum dissipation by gravitational waves, the ellipsoidal hypermassive neutron star may collapse to a black hole within ~ 50 ms, as found in [21], even in the absence of any other transport mechanism. On the other hand, if the ellipticity reduces to zero within ~ 50 ms, the hypermassive neutron star will settle to a spheroid in a stationary state. Then, the collapse to a black hole will be triggered by other mechanisms such as the magnetic braking and the MRI [55, 56, 57].

Since a torque works from the ellipsoidal hypermassive neutron star, matter in the outer envelop receives angular momentum from the central part. This process helps producing disk, which may be an accretion disk around a black hole eventually formed. If gravitational radiation triggers the collapse, the expected disk mass is $\sim 0.01\text{--}0.03M_{\odot}$ for merger of equal-mass as well as unequal-mass binaries for $Q_M \gtrsim 0.85$ with the black hole mass $\sim 2.6\text{--}2.8M_{\odot}$ and spin $q < 0.7$. Such system may be a central engine of SGRBs of relatively small burst energy [64, 67].

Alternatively, collapse to a black hole may be triggered by other mechanisms such as the magnetic braking and the MRI [55, 56, 57]. In the collapse by these magnetic effects, the mass of a torus surrounding the black hole will be larger than $0.05M_{\odot}$ because an efficient angular momentum transport works, as illustrated in [56, 57]. Furthermore, the MRI generates shocks in the torus, heating up the material to $\sim 10^{11}$ K [57]. Therefore, this scenario is more favorable for producing a central engine of SGRBs.

If the time scale of the angular momentum transport in the hypermassive neutron stars is longer than ~ 50 ms, a black hole or a spheroidal hypermassive neutron star is formed after a longterm emission of quasiperiodic gravitational waves. Such gravitational waves may be detected by advance laser-interferometric detectors (see summary 6). If a black hole is subsequently formed, it may also produce a SGRB. Thus, if quasiperiodic gravitational waves and subsequent SGRB are detected coincidently in the

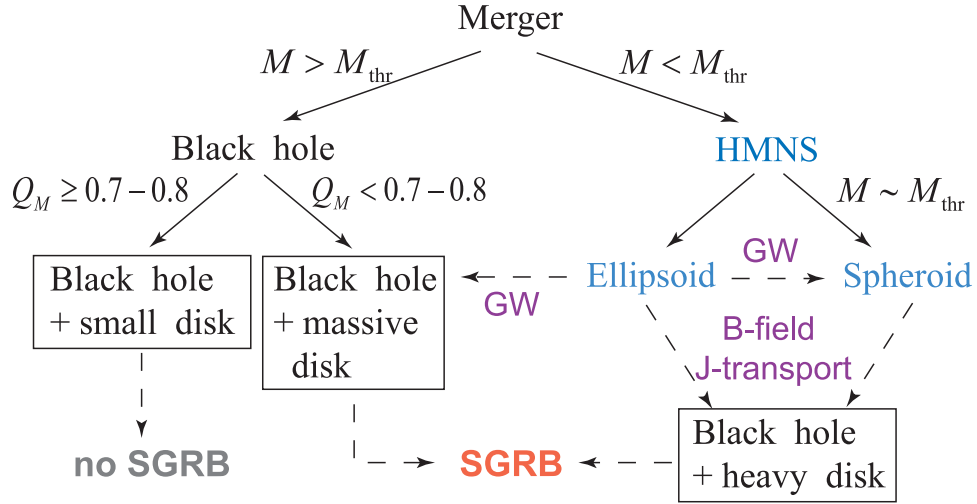


FIG. 21: Summary about the outcome after the merger. “HMNS”, “GW”, “B-field”, and “J-transport” are hypermassive neutron star, gravitational wave emission, magnetic field, and angular momentum transport, respectively. “small disk”, “massive disk”, and “heavy disk” imply that the disk mass is $M_d \ll 0.01M_\odot$, $0.01M_\odot \lesssim M_d \lesssim 0.03M_\odot$, and $M_d \gtrsim 0.05M_\odot$, respectively. The solid arrow denotes the route found in this paper and the dashed arrow is the possible route based on the results of [57] and the speculation. There are three possible fates of the ellipsoidal hypermassive neutron star depending on the EOS and the time scale of dissipation and angular momentum transport processes. We note that a spheroid is formed probably only for the APR EOS. See the summary 1–4 for details.

same direction with small time lag, the merger scenario through formation of a hypermassive neutron star for the central engine of SGRBs may be confirmed. (However, for detecting gravitational waves, the event should be within ~ 50 Mpc; see summary 6).

In the presence of strong magnetic fields with $\gtrsim 10^{16}$ G, a black hole may be formed before a longterm emission of quasiperiodic gravitational waves from the hypermassive neutron star [56, 57]. In this case, a smaller value of h_{eff} for the quasiperiodic gravitational waves is expected, and hence, a smaller-distance event is required for confirmation of this scenario by gravitational wave detection.

3. Formation of hypermassive neutron star ($M \lesssim M_{\text{thr}}$)

For M only slightly smaller than M_{thr} , the hypermassive neutron star relaxes to a spheroidal state in ~ 10 ms since its small angular momentum and compact structure lead to a too small ratio of the rotational kinetic energy to the gravitational binding energy to form an ellipsoid [58]. Here, the small angular momentum is a result from the effects that the angular momentum is significantly dissipated by gravitational waves soon after the onset of the merger and that the angular momentum transport works efficiently during an early quasiradial oscillation with a large amplitude in the hypermassive neutron star. Since the emissivity of gravitational waves by the hypermassive neutron stars of small ellipticity is not high, it may survive for more than 50 ms in contrast to the smaller-mass case. Collapse to a black hole will be triggered by other mechanism such as the magnetic braking and the MRI [55, 56, 57]. After the collapse, disk of mass $\gtrsim 0.05M_\odot$ could be formed [56, 57], and hence, such system is also a candidate for the central engine of SGRBs.

In this scenario, the amplitude of quasiperiodic gravitational waves is not as high as that for the smaller-mass case, and hence, frequent detection of this signal is not expected (see summary 6).

The formation of a spheroid is found only for the APR EOS (in [21] in which the SLy and FPS EOSs are used, we have not found the formation of spheroids). The likely reason in this difference is that the APR EOS is stiffer than others. Namely, the hypermassive neutron stars can be more compact with this EOS [cf. Fig. 2(b)] escaping the collapse to a black hole. In such compact state, the gravitational binding energy could be large enough to reduce the ratio of the rotational kinetic energy to the binding energy below the threshold value of the formation of an ellipsoid.

4. Prompt formation of black hole ($M > M_{\text{thr}}$)

In the black hole formation from the nearly equal-mass merger, most of mass elements are swallowed into the horizon, and hence, the disk mass around the black hole is much smaller than $0.01M_\odot$. However, the disk mass steeply increases with decreasing the value of Q_M ; we find an empirical relation in which the disk mass is written approximately by $M_{d0} + M_{d1}(1 - Q_M)^p$ with $p = 3-4$ for given EOS and mass for a range $0.7 \lesssim Q_M \leq 1$.

For $Q_M \sim 1$, the disk not only has small mass but also is geometrically thin. Therefore, the merger will not produce a central engine of SGRBs for nearly equal-mass case. On the other hand, for a sufficiently small value of Q_M ($Q_M \lesssim 0.75$ for the APR EOS and $Q_M \lesssim 0.85$ for the SLy EOS), the disk mass is larger than $0.01M_\odot$. Furthermore, the disk is geometrically thick and the thermal energy is large enough (typically $\sim 1-2 \times 10^{11}$ K)

for producing the large amount of thermal neutrinos. In addition, the black hole spin is large $q \sim 0.75$. Therefore, prompt formation of a black hole in the merger of unequal-mass binary neutron stars with a small value of Q_M is a scenario for formation of a central engine of SGRBs. Unfortunately, binary neutron stars of small mass ratio with $Q_M < 0.9$ have not been found so far [49]. Hence, it is not clear at present whether the merger rate of such unequal-mass binary is large enough for explaining the event rate of SGRBs. The present results also indicate that the merger between a neutron star and a black hole with small mass will be a possible candidate for producing central engine of SGRBs.

5. Gravitational waves from black hole

The non-dimensional angular momentum parameter (J/M^2) of the formed Kerr black hole is ~ 0.75 in the prompt formation case. Then, for the system of mass $2.7\text{--}2.9M_\odot$, the frequency of ring-down gravitational waves associated with the fundamental quasinormal mode of $l = m = 2$ is $\sim 6.5\text{--}7$ kHz. We extract the ring-down gravitational waveform and confirm this frequency. The amplitude of gravitational waves is $\sim 1\text{--}2 \times 10^{-22}$ at a distance of 50 Mpc which is too small to be detected even by advanced laser-interferometric detectors unless the merger event happens within the local group of galaxies.

6. Gravitational waves from hypermassive neutron star

The effective amplitude of quasiperiodic gravitational

waves from hypermassive neutron stars of ellipsoidal shape can be $\gtrsim 5 \times 10^{-21}$ at a distance of 50 Mpc with the frequency 3–3.5 kHz. This property agrees with that found in [21, 24], and hence, we conclude that this fact holds irrespective of stiff nuclear EOSs with $M_{\text{sph}} \gtrsim 2M_\odot$. Quasiperiodic gravitational waves may be detected by advanced laser-interferometric detectors. Detection will lead to constraining the nuclear EOS as discussed in [24]. On the other hand, for M only slightly smaller than M_{thr} , the expected effective amplitude is $h_{\text{eff}} \sim 2 \times 10^{-21}$ at a distance of 50 Mpc with frequency $f \sim 4$ kHz; only for an event with a distance within ~ 10 Mpc, detection of such signal will be possible by the advanced laser-interferometric detectors.

Acknowledgments

MS is grateful to Stu Shapiro for discussion about the fate of hypermassive massive neutron stars during collaboration in the magnetohydrodynamic simulation in general relativity. Numerical computations were performed on the FACOM VPP5000 machine at the data analysis center of NAOJ and on the SX6 machine at the data analysis center of ISAS in JAXA. This work was in part supported by Monbukagakusho Grant (Nos. 17030004 and 17540232).

-
- [1] M. Burgey et al., *Nature* **426**, 531 (2003).
 - [2] V. Kalogera et al., *Astrophys. J.* **601**, L179 (2004); *ibid.*, **614**, L137 (2004).
 - [3] C. Cutler and K. S. Thorne, in *Proceedings of the 16th International Conference on General Relativity and Gravitation*, eds. N. T. Bishop and S. D. Maharaj (World Scientific, 2002), p.72, and references therein.
 - [4] M. Ando et al. (the TAMA collaboration), *Phys. Rev. Lett.* **86**, 3950 (2001).
 - [5] R. Narayan, B. Paczynski, and T. Piran, *Astrophys. J. Lett.* **395**, L83 (1992).
 - [6] B. Zhang and P. Mészáros, *Int. J. Mod. Phys. A* **19**, 2385 (2004); T. Piran, *Rev. Mod. Phys.* **76**, 1143 (2005).
 - [7] J. S. Bloom, et al., *Astrophys. J.* **638**, 354 (2006); N. Gehrels, et al., *Nature*, **437**, 851 (2005); E. Berger et al., *Nature*, **438**, 988 (2005); S. D. Barthelmy et al., *Nature*, **438**, 994 (2005).
 - [8] D. B. Fox, et al., *Nature*, **437**, 845 (2005).
 - [9] J. S. Villaseñor, et al., *Nature*, **437**, 855 (2005); J. Hjorth, et al., *Nature*, **437**, 859 (2005).
 - [10] E.g., M. Ruffert and H.-Th. Janka, *Astron. Astrophys.* **380**, 544 (2001).
 - [11] M. Shibata, *Phys. Rev. D* **60**, 104052 (1999).
 - [12] M. Shibata and K. Uryū, *Phys. Rev. D* **61**, 064001 (2000).
 - [13] M. Shibata and K. Uryū, *Prog. Theor. Phys.* **107**, 265 (2002).
 - [14] J. A. Font et al., *Phys. Rev. D* **65**, 084024 (2002).
 - [15] J. A. Font, *Living Rev. Relativ.* **6**, 4 (2003).
 - [16] M. Shibata, *Phys. Rev. D* **67**, 024033 (2003).
 - [17] M. Shibata, K. Taniguchi, and K. Uryū, *Phys. Rev. D* **68**, 084020 (2003).
 - [18] M. Miller, P. Gressman, and W.-M. Suen, *Phys. Rev. D* **69**, 064026 (2004).
 - [19] M. D. Duez, P. Marronetti, T. W. Baumgarte, and S. L. Shapiro, *Phys. Rev. D* **67**, 024004 (2003).
 - [20] L. Baiotti, I. Hawke, P. J. Montero, F. Löffler, L. Rezzolla, N. Stergioulas, J. A. Font, and E. Seidel, *Phys. Rev. D* **71**, 024035 (2005).
 - [21] M. Shibata, K. Taniguchi, and K. Uryū, *Phys. Rev. D* **71**, 084021 (2005).
 - [22] The hypermassive neutron star is defined as a differentially rotating neutron star for which the total baryon rest-mass is larger than the maximum allowed value of rigidly rotating neutron stars for a given EOS: See [23] for definition.
 - [23] T. W. Baumgarte, S. L. Shapiro, and M. Shibata, *Astrophys. J. Lett.* **528**, L29 (2000).
 - [24] M. Shibata, *Phys. Rev. Lett.* **94**, 201101 (2005).
 - [25] D. J. Nice et al., *Astrophys. J.*, **634**, 1242 (2005).
 - [26] A. Akmal, V. R. Pandharipande, and D. G. Ravenhall, *Phys. Rev. C* **58**, 1804 (1998).
 - [27] F. Douchin and P. Haensel, *Astron. Astrophys.* **380**, 151 (2001).
 - [28] W. Unruh, unpublished (1984); E. Seidel and W.-M. Suen, *Phys. Rev. Lett.* **69**, 1845 (1992).
 - [29] M. Alcubierre and B. Brügmann, *Phys. Rev. D* **63**,

- 104006 (2001).
- [30] M. D. Duez, S. L. Shapiro, and H.-J. Yo, Phys. Rev. D. **69**, 104016 (2004).
 - [31] R. Oechslin and H.-Th. Janka, Mon. Not. R. astr. Soc., submitted (astro-ph/0507099).
 - [32] H. Shen, H. Toki, K. Oyamatsu, and K. Sumiyoshi, Nuclear physics A **637**, 435 (1998).
 - [33] M. Shibata and T. Nakamura, Phys. Rev. D **52** (1995), 5428; see also, T. W. Baumgarte and S. L. Shapiro, Phys. Rev. D **59** (1999), 024007; M. Alcubierre et al., Phys. Rev. D **61** (2000), 041501.
 - [34] A. Kurganov and E. Tadmor, J. Comput. Phys. **160**, 214 (2000).
 - [35] M. Shibata and J. A. Font, Phys. Rev. D **72**, 047501 (2005).
 - [36] M. Shibata, Prog. Theor. Phys. **101**, 1199 (1999).
 - [37] M. Shibata, Astrophys. J. **595**, 992 (2003).
 - [38] M. Shibata, Phys. Rev. D **55**, 2002 (1997); M. Shibata and K. Uryū, Phys. Rev. D **62**, 087501 (2000).
 - [39] J. R. Wilson and G. J. Mathews, Phys. Rev. Lett. **75**, 4161 (1995).
 - [40] C. S. Kochanek, Astrophys. J. **398**, 234 (1992); L. Bildsten and C. Cutler, Astrophys. J. **400**, 175 (1992).
 - [41] M. Shibata, Phys. Rev. D **58**, 024012 (1998).
 - [42] S. A. Teukolsky, Astrophys. J. **504**, 442 (1998).
 - [43] E. Gourgoulhon et al., Phys. Rev. D **63**, 064029 (2001).
 - [44] K. Taniguchi and E. Gourgoulhon, Phys. Rev. D **66**, 104019 (2002); *ibid* **68**, 124025 (2003).
 - [45] V. Moncrief, Ann. of Phys. **88**, 323 (1974): The Moncrief formalism was originally derived for the Schwarzschild spacetime. We here apply his formalism in a flat space-time.
 - [46] M. Shibata and Y.I. Sekiguchi, Phys. Rev. D **71**, 024014 (2005).
 - [47] P. Haensel and A. Y. Potekhin, Astron. Astrophys. **428**, 191 (2004).
 - [48] The tables for the SLy and APR EOSs, which were involved in the LORENE library in Meudon group (<http://www.lorene.obspm.fr>), were implemented by Haensel and Zdunik. (See [81] for quasiequilibrium sequences of binary neutron stars using these tables.)
 - [49] S. Chandrasekhar, *Stellar Structure* (Dover, 1967), Chap. 10.
 - [50] I. H. Stairs, Science **304**, 547 (2004).
 - [51] S. Tsuruta, Phys. Rep. **292**, 1 (1998).
 - [52] K. Uryū, M. Shibata, and Y. Eriguchi, Phys. Rev. D **62**, 104015 (2000).
 - [53] M. Shibata and K. Uryū, Phys. Rev. D **64**, 104017 (2001).
 - [54] N. D. Lyford, T. W. Baumgarte, and S. L. Shapiro, Astrophysical J. **583**, 410 (2003); I. A. Morrison, T. W. Baumgarte, and S. L. Shapiro, Astrophys. J. **610**, 941 (2004).
 - [55] M. Shibata, T. W. Baumgarte, and S. L. Shapiro, Astrophys. J. **542**, 453 (2000).
 - [56] S. A. Balbus and J. F. Hawley, Astrophys. J. **376**, 214 (1991); Rev. Mod. Phys. **70**, 1 (1998).
 - [57] M. D. Duez, Y. T. Liu, S. L. Shapiro, M. Shibata, and B. C. Stephens, Phys. Rev. Lett. **96**, 031101 (2006).
 - [58] M. Shibata, M. D. Duez, Y. T. Liu, S. L. Shapiro, and B. C. Stephens, Phys. Rev. Lett. **96**, 031102 (2006).
 - [59] S. Chandrasekhar, *Ellipsoidal Figures of Equilibrium* (Yale University Press, New Haven, 1969); J.-L. Tassoul, *Theory of Rotating Stars* (Princeton Univ. Press, Princeton, 1978).
 - [60] J. M. Bardeen, W. H. Press, and S. A. Teukolsky, Astrophys. J. **178**, 347 (1972).
 - [61] M. Ruffert, H.-Th. Janka, and G. Schäfer, Astron. Astrophys. **311**, 532 (1996); M. Ruffert et al., *ibid* **319**, 122 (1997); H.-Th. Janka and M. Ruffert, Astron. Astrophys. **307**, L33 (1996).
 - [62] M. Berger and J. Oliger, J. Comp. Phys. **53**, 484 (1984); E. Evans, S. Iyer, E. Schnetter, W.-M. Suen, J. Tao, R. Wolfmeyer, and H.-M. Zhang, Phys. Rev. D **71**, 081301 (2005); B. Zink, N. Stergioulas, I. Hawke, C. D. Ott, E. Schnetter, and E. Müller, gr-qc/0501080.
 - [63] E. W. Leaver, Proc. R. Soc. London **A402**, 285 (1985). T. Nakamura, K. Oohara, and Y. Kojima, Prog. Theor. Phys. Suppl. No. **90**, 1 (1987).
 - [64] I. D. Novikov and K. S. Thorne, in *Black Holes*, edited by B. DeWitt and C. DeWitt (Gordon Breach, New York, 1973).
 - [65] R. Popham, S. E. Woosley, and C. Fryer, Astrophys. J. **518**, 356 (1999).
 - [66] R. Narayan, T. Piran, and P. Kumar, Astrophys. J. **557**, 949 (2001).
 - [67] K. Kohri and S. Mineshige, Astrophys. J. **577**, 311 (2002).
 - [68] Di Matteo, R. Perna, and R. Narayan, Astrophys. J. **579**, 706 (2002).
 - [69] S. Setiawan, M. Ruffert, and H.-Th. Janka, Mon. Not. R. astr. Soc. **352**, 753 (2004).
 - [70] W. H. Lee, E. R. Ruiz, and D. Page, Astrophys. J. **608**, L5 (2004); Astrophys. J. **632**, 421 (2005).
 - [71] See, e.g., Appendix I of S. L. Shapiro and S. A. Teukolsky, *Black Holes, White Dwarfs, and Neutron Stars*, Wiley Interscience (New York, 1983).
 - [72] R. Takahashi, private communication.
 - [73] M. A. Aloy, H.-T. Janka, and E. Müller, Astron. Astrophys. **436**, 273 (2005).
 - [74] J. A. Faber, T. W. Baumgarte, S. L. Shapiro, K. Taniguchi, and F. A. Rasio, Phys. Rev. D **73**, 024012 (2006).
 - [75] M. Ishii, M. Shibata, and Y. Mino, Phys. Rev. D **71**, 044017 (2005). See also, [82].
 - [76] L. Blanchet, G. Faye, B. R. Iyer, and B. Joguet, Phys. Rev. D **65**, 061501(R) (2002); L. Blanchet, T. Damour, G. Esposito-Farese, and B. R. Iyer, Phys. Rev. Lett. **93**, 091101 (2004).
 - [77] It is important to check that the quasinormal mode of a black hole is seen for $t_{\text{ret}} \gtrsim t_{\text{AH}}$ for confirming that it is different from the w-mode [77] which has a similar damping waveform but is emitted before the formation of a black hole. For example, see [78] in which the authors seem to misrelate the gravitational waveform extracted to a quasinormal mode ringing; namely, the gravitational waveform is extracted only for $t_{\text{ret}} < t_{\text{AH}}$ in their simulation, and hence, it cannot correspond to a quasinormal mode of a black hole.
 - [78] N. Andersson and K. D. Kokkotas, Phys. Rev. Lett. **77**, 4134 (1996); K. D. Kokkotas and B. Schmidt, Living Rev. Relativ. **2**, 2 (1999).
 - [79] L. Baiotti, I. Hawke, L. Rezzolla, and E. Schnetter, Phys. Rev. Lett. **94**, 131101 (2005).
 - [80] F. A. Rasio and S. L. Shapiro, Astrophys. J. **432**, 242 (1994); X. Zhuge, J. M. Centrella, and S. L. W. McMillan, Phys. Rev. D **54**, 7261 (1996).
 - [81] J. A. Faber and F. A. Rasio, Phys. Rev. D **62**, 064012 (2000); *ibid* **63**, 044012 (2001); *ibid* **65**, 084042 (2002).

- [81] M. Bejger, D. Gondek-Rosińska, E. Gourgoulhon, P. Haensel, K. Taniguchi, and J.L. Zdunik, *Astron. Astrophys.* **431**, 297 (2005).
- [82] K. Taniguchi, T. W. Baumgarte, J. A. Faber, S. L. Shapiro, *Phys. Rev. D* **72**, 044008 (2005).